ORBITAL FLOW PAST A CYLINDER: A NUMERICAL APPROACH

A. BORTHWICK*

Department of Civil Engineering, University of Salford, Salford M5 4WT, U.K.

SUMMARY

Orbital flow past a cylinder is relevant to offshore structures. The numerical scheme presented here is based on a finite-difference solution of the Navier–Stokes equations. Alternating-directional-implicit (ADI) and successive-over-relaxation (SOR) techniques are used to solve the vorticity-transport and stream-function equations. Theoretical simulations to low Reynolds number flows (up to 1000) are discussed for cases involving uniform flow past stationary and rotating cylinders and orbital flow past a cylinder. The separation points for cylinders that are rotating or immersed in an orbital flow are deduced from velocity profiles through the boundary layer using a hybrid mesh scheme. During the initial development of orbital flow surface vorticity on the impulsively started cylinder dominates the flow. A vortex then detaches from behind the cylinder and establishes the flow pattern of the orbit. After some time a collection of vortices circles the orbit and distorts its shape a great deal. These vortices gradually spiral outward as others detach from the cylinder and join the orbital path.

INTRODUCTION

Design of offshore structures is much influenced by the wave loading on component members. These consist usually of tubular cylinders. Plane oscillatory flow provides a reasonable analogy to the flow experienced by a horizontal cylinder under regular small amplitude wave loading very close to the ocean bed where particle orbits are almost flat ellipses. Away from the bottom, particle orbits form more rounded ellipses and close to the free surface they may become nearly circular.

For numerical simulation of flow past a cylinder, two main methods have been developed in the past. One is based on superimposing discrete vortices onto a potential flow solution. The other involves a finite-difference approximation to the time-dependent Navier–Stokes equations. Although this method is limited to low Reynolds number flows and is expensive as regards computer resources, it is free from empiricism. A finite-difference approach is used in this paper.

A brief review of the historical development of Navier–Stokes finite-difference models has been given by Borthwick.[1,2]

The main disadvantage of the Navier–Stokes finite-difference method is that it can only be applied with justification to low Reynolds number cases where the flow is laminar. Turbulence is not modelled, and would present problems beyond the scope of this paper to include. Therefore the solutions are limited here to Reynolds numbers less than 1000. Although the method gives a more
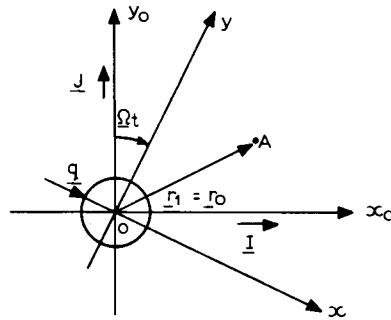
---

* Lecturer

Figure 1. Cylinder immersed in an orbital flow

exact theoretical answer, it is more complicated than the potential flow model, with an impracticably small mesh required in some cases.

Stansby[3,4] has developed and improved numerical solutions of steady and planar oscillatory flows past a cylinder using discrete vortex models. He assumed that the separation points were fixed close to the cylinder centre plane to the incident velocity. Lack of information about separation and the accumulation of vast numbers of vortices cause major empirical problems in these discrete vortex oscillating flow models.

As far as can be ascertained a Navier–Stokes finite-difference simulation has not been applied previously to either planar oscillatory flow or circular orbital flow problems.

FUNDAMENTAL EQUATIONS

In studying orbital flow past a rotating cylinder it is convenient to consider a rotating frame of reference. The absolute acceleration

$$\frac{D\mathbf{q}}{Dt} = \frac{\partial \mathbf{q}}{\partial t} + V_r \frac{\partial \mathbf{q}}{\partial r} + \frac{V_\theta}{r} \frac{\partial \mathbf{q}}{\partial \theta}, \qquad \text{where} \quad \mathbf{q} = \begin{bmatrix} V_r \\ V_\theta \end{bmatrix}, \tag{1}$$

must be expressed in terms of derivatives of the relative velocities as discussed by Raudkivi and Callander.[5]

Figure 1 illustrates orbital flow past a rotating cylinder, where the centres of the inertial and moving frames of reference coincide. This is equivalent to the flow around a horizontal cylinder under regular deep water small amplitude waves where particle orbits are almost circular. Neglecting the decrease in magnitude of velocity components with depth and the slight forward progression of the particle orbits with time, a constant velocity vector rotates with uniform angular speed around the cylinder.

For the experimental work undertaken by Holmes and Chaplin[6] and Borthwick[1] a frame of reference was chosen so that the cylinder revolves around a circular orbit while rotating on its own axis, as shown in Figure 2. In the diagram, the unit vectors **I** and **J** act in the x_0 and y_0 directions respectively. Then

$$\mathbf{R} = \mathbf{I}R \cos \Omega t + \mathbf{J}R \sin \Omega t. \tag{2}$$

It is now possible to write the Navier–Stokes equations in polar co-ordinates for this frame of reference. From continuity,

$$\operatorname{div} \mathbf{q} = V_r + r \frac{\partial V_r}{\partial r} + \frac{\partial V_\theta}{\partial \theta} = 0. \tag{3a}$$
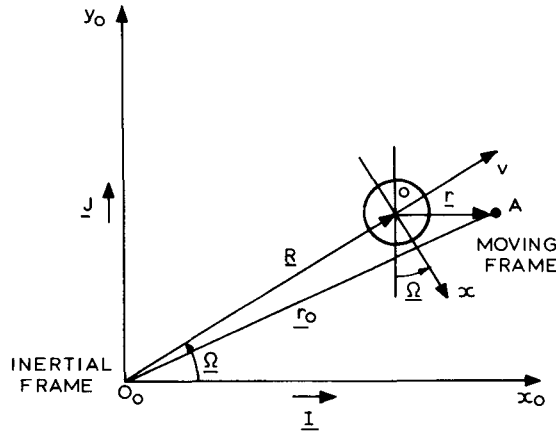
Figure 2. Inertial and moving frames of reference for a rotating cylinder revolving around a circular orbit

The radial and tangential momentum components are

$$\rho\left[\frac{\partial V_r}{\partial t} + V_r\frac{\partial V_r}{\partial r} + \frac{V_\theta}{r}\frac{\partial V_r}{\partial \theta} - \frac{V_\theta^2}{r} - \Omega^2 R\sin\theta - \Omega^2 r - 2\Omega V_\theta\right]$$

$$= -\frac{\partial P}{\partial r} + \mu\left[\frac{1}{r}\frac{\partial}{\partial r}\left(r\frac{\partial V_r}{\partial r}\right) + \frac{1}{r^2}\frac{\partial^2 V_r}{\partial \theta^2} - \frac{V_r}{r^2}\frac{\partial V_\theta}{\partial \theta}\right] \qquad (3b)$$

and

$$\rho\left[\frac{\partial V_\theta}{\partial t} + V_r\frac{\partial V_\theta}{\partial r} + \frac{V_\theta}{r}\frac{\partial V_\theta}{\partial \theta} + \frac{V_\theta V_r}{r} - \Omega^2 R\cos\theta + 2\Omega V_r\right]$$

$$= -\frac{1}{r}\frac{\partial P}{\partial \theta} + \mu\left[\frac{1}{r}\frac{\partial}{\partial r}\left(r\frac{\partial V_\theta}{\partial r}\right) + \frac{1}{r^2}\frac{\partial^2 V_\theta}{\partial \theta^2} - \frac{V_\theta}{r^2} + \frac{2}{r^2}\frac{\partial V_r}{\partial \theta}\right]. \qquad (3c)$$

Letting $r' = r/r_a$, $V_r' = V_r/U_\infty$, $V_\theta' = V_\theta/U_\infty$, $t' = tU_\infty/r_a$ and $P' = (P - P_\infty)/\rho U_\infty^2$, etc. the flow equations are non-dimensionalized. The Reynolds, Keulegan–Carpenter and Strouhal numbers are defined as

$$Re = \frac{2U_\infty r_a}{\nu}, \quad Kc = \frac{\pi U_\infty}{\Omega r_a} \quad \text{and} \quad S = \frac{2f r_a}{U_\infty}, \qquad (4)$$

respectively, where f is the vortex shedding frequency. The velocity components V_r' and V_θ' are defined as

$$V_r' = \frac{1}{r'}\frac{\partial \psi'}{\partial \theta'} \quad \text{and} \quad V_\theta' = -\frac{\partial \psi'}{\partial r'}. \qquad (5)$$

The vorticity, ω, is given as

$$\omega' = \frac{1}{r'}\left[\frac{\partial(r'V_\theta')}{\partial r'} - \frac{\partial V_r'}{\partial \theta'}\right]. \qquad (6)$$

Hence the parabolic vorticity-transport and the stream-function equations are obtained as

$$\frac{\partial \omega'}{\partial t'} + \frac{1}{r'}\frac{\partial(V_\theta'\omega')}{\partial \theta'} + \frac{1}{r'}\frac{\partial(r'V_r'\omega')}{\partial r'} = \frac{2}{Re}\left[\frac{1}{r'}\frac{\partial}{\partial r'}\left[r'\frac{\partial \omega'}{\partial r'}\right] + \frac{1}{r'^2}\frac{\partial^2 \omega'}{\partial \theta'^2}\right] \qquad (7)$$

and

$$\frac{\partial^2 \psi'}{\partial r'^2} + \frac{1}{r'}\frac{\partial \psi'}{\partial r'} + \frac{1}{r'^2}\frac{\partial^2 \psi'}{\partial \theta'^2} = -\omega'. \tag{8}$$

The above equations can be rewritten in log-polar form with the use of the transformation $r' = e^{aZ}$ and $\theta' = a\theta$. From now on the primes are ignored. Equations (5)–(8) become

$$V_r = E_z^{-1/2}\frac{\partial \psi}{\partial \theta}, \qquad V_\theta = -E_z^{1/2}\frac{\partial \psi}{\partial Z}, \tag{9a}$$

$$E_z\frac{\partial \omega}{\partial t} + \frac{\partial \omega}{\partial Z}\frac{\partial \psi}{\partial \theta} - \frac{\partial \omega}{\partial \theta}\frac{\partial \psi}{\partial Z} = \frac{2}{Re}\left[\frac{\partial^2 \omega}{\partial Z^2} + \frac{\partial^2 \omega}{\partial \theta^2}\right] \tag{9b}$$

and

$$\frac{\partial^2 \psi}{\partial Z^2} + \frac{\partial^2 \psi}{\partial \theta^2} = -E_z\omega, \tag{9c}$$

where $E_z = a^2 e^{2aZ}$.

NUMERICAL SCHEME

The domain was discretized using a coarse regular mesh and a hybrid mesh. Finite-difference approximations to the flow equations were applied at each node. The velocity components and stream function equation were adequately described by central difference approximations. An iterative process involving successive over-relaxation was used to obtain updated values of stream functions from the stream-function equation. The iterations were terminated when the difference between successive values fell below a preset error parameter. The vorticity-transport equation was solved satisfactorily by the use of an alternating-directional-implicit (ADI) approach. Spatial and temporal accuracy was achieved by varying the fineness of the mesh and using a Neumann stability criterion given by Thoman and Szewczyk.[7]

Borthwick[1,2] has already described the coarse mesh for a uniform flow problem. For this regular mesh a log-polar co-ordinate based 'rectangular' grid was used which lends itself to simple numerical treatment. Lin and Lee,[8] Son and Hanratty,[9] Martinez[10] and Thoman and Szewczyk[7] have compared results obtained for grids with various spacings of Δz and $\Delta \theta$. Lin, Pepper and Lee[11] suggested a time step, $\Delta t = 0.02$, for a similar grid to the one used here, for Reynolds numbers less than 400. As a result the discretization parameters used for the rough grid in this case are $\Delta Z = \Delta \theta = \pi/45$ and $\Delta t = 0.02$.

The coarse mesh is unsatisfactory because of the enormous number of points required to model the conditions within the boundary layer while ensuring that the outer boundary is located at such a distance that it has no effect on the near wake. Therefore a hybrid mesh similar to that devised by Thoman and Szewczyk[7] is also used, in which the flow region is divided into inner and outer flow areas.

The inner flow region extends from the surface of the cylinder outward until it blends into the outer flow mesh. This inner region is divided into cylindrical cells of constant angular increments $\Delta\theta = \pi/45$, but with varying radial increments. The initial radial increment is sized according to the particular Reynolds number being investigated, and each successive outward increment is increased by a factor, K, to give a sensible model of the boundary layer.

Thoman and Szewczyk[7] suggest that the radial cell width at the cylinder surface should be sized to be 1/12 of the steady-state forward stagnation point boundary layer thickness. This stagnation-

thickness is defined by Schlichting[12] to be equal to $2\cdot4\, r_a/\sqrt{Re}$, where r_a is the radius of the cylinder. Thus the radial cell increment at the cylinder surface is taken as $0\cdot2/\sqrt{Re}$. The second cell has a radial increment of K times the first, and so on until the cells have reached a suitable width to blend into the outer region. A value of $1\cdot5$ for K was found by Thoman and Szewczyk to be adequate for their computations and is adopted here.

The very fine definition near the cylinder surface is achieved without the penalty of requiring a small computing time increment for stability because the maximum radial velocity component is very small near the cylinder surface.

The outer region is composed of a cylindrical mesh which becomes a Cartesian mesh in the log-polar domain. The position of the outer boundary is at least 80 radii from the centre of the cylinder.

FINITE-DIFFERENCE QUOTIENTS

The method of finite-difference quotients proposed by Schlichting[12] is used to approximate the flow equations in polar form when applied to the inner region until it blends with the outer region. For the inner region, which encompasses the boundary layers, spatial accuracy is improved from order $(\Delta\theta^2, \Delta Z^2)$ using central differences to order $(\Delta\theta^2, \Delta r^2)$ using finite quotients. This is a major advantage of using finite quotients. In the outer region the flow characteristics vary more slowly and so the same method as used for the regular mesh scheme given by Borthwick[1,2] is chosen. In the outer region the flow equations are expressed in log-polar form and approximated by central differences.

The finite-quotient formulation is now described for part of the inner grid, close to the cylinder surface. This is shown in Figure 3 where $\Delta\theta$ is the constant angular increment and $\overline{\Delta r_j}$ is the varying radial cell increment. From the properties of the grid the formulae given below are known:

$$r_1 = 1, \quad r_j = r_1 + \frac{\Delta r_1}{k'}(K^{j-1} - 1), \qquad \text{where} \quad k' = K - 1$$

and

$$K = \frac{\Delta r_j}{\Delta r_{j-1}}; \quad \overline{\Delta r_j} = \tfrac{1}{2}[\Delta r_j + \Delta r_{j-1}], \quad j = 2, \ldots, M - 1. \tag{10}$$
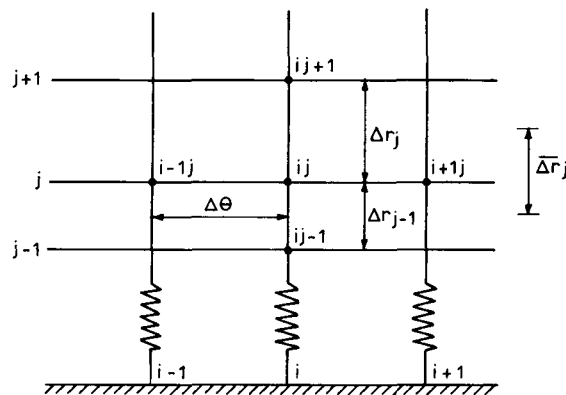

Figure 3. Diagram showing part of inner grid

Schlichting[12] obtained the following finite-quotient approximations for the derivatives of a function f at the point i,j:

$$\left.\frac{\partial f}{\partial \theta}\right|_{ij} = \frac{f_{i+1j} - f_{i-1j}}{2\Delta\theta}; \quad \left.\frac{\partial^2 f}{\partial \theta^2}\right|_{ij} = \frac{f_{i+1j} + f_{i-1j} - 2f_{ij}}{\Delta\theta^2},$$

$$\left.\frac{\partial f}{\partial r}\right|_{ij} = \frac{1}{2\Delta r_j}\{L_3 f_{ij-1} + L_2 f_{ij} + L_1 f_{ij+1}\}, \tag{11}$$

where

$$L_1 = K^{-1}, \quad L_2 = (K^2 - 1)L_1, \quad L_3 = -K,$$

and

$$\left.\frac{\partial^2 f}{\partial r^2}\right|_{ij} = \frac{P}{\Delta r_j^2}\{P_4 f_{ij-1} - P_3 f_{ij} + P_2 f_{ij+1}\}, \tag{12}$$

where

$$P_1 = \tfrac{1}{2}(K+1), \quad P_2 = L_1, \quad P_3 = 2P_1 P_2, \quad P_4 = 1.$$

The point at which the inner mesh blends with the outer is defined as $j = \text{NOJ}$. It should be noted that K does not equal the fixed value of 1·5, but is equal to $\Delta r_{\text{NOJ}-1}/\Delta r_{\text{NOJ}-2}$ when $j = \text{NOJ} - 1$.

SOLUTION OF THE STREAM-FUNCTION EQUATION

The stream-function equation is rewritten in finite-difference form as

$$\psi_{ij} := \{2r_j^2 \overline{\Delta r_j^2} \Delta\theta^2 \omega_{ij} + r_j \Delta\theta^2 (2r_j P_1 + \overline{\Delta r_j} L_3)\psi_{ij-1}$$
$$+ r_j \Delta\theta^2 (r_j P_3 + \overline{\Delta r_j} L_1)\psi_{ij+1} + \overline{2\Delta r_j^2}(\psi_{i+1j} + \psi_{i-1j})\}/(P_1 P_3 2r_j^2 \Delta\theta^2 - L_2 r_j \Delta\theta^2 \overline{\Delta r_j}$$
$$+ 4\overline{\Delta r_j^2}), \quad j = 2,\ldots,\text{NOJ} - 1$$

for the inner mesh, and

$$\psi_{ij} := \left\{E_z \omega_{ij} + \frac{\psi_{ij+1}}{\Delta Z^2} + \frac{\psi_{ij-1}}{\Delta Z^2} + \frac{\psi_{i+1j}}{\Delta\theta^2} + \frac{\psi_{i-1j}}{\Delta\theta^2}\right\} \bigg/ \left(\frac{2}{\Delta Z^2} + \frac{2}{\Delta\theta^2}\right), \quad j = \text{NOJ},\ldots,M-1 \tag{13}$$

for the outer mesh. This is solved iteratively, using the method of successive over-relaxation.

CALCULATION OF VELOCITIES

The radial and angular velocity components may be expressed using appropriate finite-difference approximations as

$$V_{r_{ij}} = \frac{\psi_{i+1j} - \psi_{i-1j}}{2\Delta\theta r_j}, \quad j = 2,\ldots,\text{NOJ} - 1,$$

$$V_{r_{ij}} = \frac{\psi_{i+1j} - \psi_{i-1j}}{2\Delta\theta E_z^{1/2}}, \quad j = \text{NOJ},\ldots,M-1,$$

and

$$V_{\theta_{ij}} = \frac{-1}{2\Delta r_j}\{L_3\psi_{ij-1} + L_2\psi_{ij} + L_1\psi_{ij+1}\}, \quad j = 2,\dots,\mathrm{NOJ}-1,$$

$$V_{\theta_{ij}} = \frac{-\psi_{ij+1} - \psi_{ij-1}}{2\Delta Z E_z^{1/2}}, \quad j = \mathrm{NOJ},\dots,M-1. \tag{14}$$

EVALUATION OF TIME STEP

For the solution of parabolic equations, such as the vorticity-transport equation, Roache[13] recommends the use of a von Neumann stability criterion, like that proposed by Thoman and Szewczyk,[7] for the time step. The condition suggested by Thoman and Szewczyk relies on the cell Reynolds number Re_c, and can be written

$$dt \leqslant \text{smallest value of} \quad \left(\frac{2Re}{d_{ij}(4 + Re_c)}\right), \quad j = 2,\dots,M-1,$$

where

$$Re_c = \frac{2Re}{d_{ij}}\left\{\left|\frac{V_{\theta_{ij}}}{\Delta\theta}\right| + \left|\frac{V_{r_{ij}}}{\Delta r_j}\right|\right\}, \quad j = 2,\dots,\mathrm{NOJ}-1,$$

$$Re_c = \frac{2Re}{d_{ij}}\left\{\left|\frac{V_{\theta_{ij}}}{\Delta\theta}\right| + \left|\frac{V_{r_{ij}}}{\Delta Z}\right|\right\}, \quad j = \mathrm{NOJ},\dots,M-1$$

and

$$d_{ij} = \frac{2}{\Delta\theta^2} + \frac{2}{\Delta r_j\Delta r_{j-1}}, \quad j = 2,\dots,\mathrm{NOJ}-1, \tag{15}$$

$$d_{ij} = \frac{2}{\Delta\theta^2} + \frac{2}{\Delta Z^2}, \quad j = \mathrm{NOJ},\dots,M-1.$$

In order to ensure stability the actual time step used is $\Delta t = 0{\cdot}8\,dt$.

THE VORTICITY-TRANSPORT EQUATION

Thoman and Szewczyk recommend the use of an 'upwind' differencing method to approximate the advective terms in the vorticity-transport equation. However, the application of this approach gives unsatisfactory results, as shown by Borthwick[1,2] where artificial viscosity damps out vortex shedding. Therefore an alternating-directional-implicit (ADI) scheme is used for the computations included in this paper.

The ADI method was first developed by Peaceman and Rachford[14] and an optimized procedure suggested by Wachpress.[15] Several authors, such as Dey,[16] Spalding,[17] Runchall[18] and Ha Minh et. al.[19] have discussed the ADI method in detail. Dey[16] showed that stability criteria are not violated up to high Reynolds numbers. Spalding[17] and Runchall[18] proposed an improved method based on the local Péclet number (i.e. the cell Reynolds number, Re_c).

In the ADI method used here, equation (7), which governs vorticity transport, is decoupled numerically to give

$$\frac{Re}{2}\left[r\frac{\omega^{k+1/2}-\omega^k}{\delta t/2}-\left(\frac{\partial\psi^k}{\partial r}\left(\frac{\partial\omega}{\partial\theta}\right)^{k+1/2}\right)\frac{1}{r}\frac{\partial^2\omega}{\partial\theta^2}\right]^{k+1/2}$$

$$=-\frac{Re}{2}\left(\frac{\partial\omega}{\partial r}\right)^k\left(\frac{\partial\psi}{\partial\theta}\right)^k+r\left(\frac{\partial^2\omega}{\partial r^2}\right)^k+\left(\frac{\partial\omega}{\partial r}\right)^k \tag{16a}$$

and

$$\frac{Re}{2}\left[r\left(\frac{\omega^{k+1}-\omega^{k+1/2}}{\delta t/2}\right)+r\left(\frac{\partial\psi}{\partial\theta}\right)^k\left(\frac{\partial\omega}{\partial r}\right)^{k+1}\right]-r\left(\frac{\partial^2\omega}{\partial r^2}\right)^{k+1}-\left(\frac{\partial\omega}{\partial r}\right)^{k+1}$$

$$=\frac{Re}{2}\left(\frac{\partial\psi}{\partial r}\right)^k\left(\frac{\partial\omega}{\partial\theta}\right)^{k+1/2}+\frac{1}{r}\left(\frac{\partial^2\omega}{\partial\theta^2}\right)^{k+1/2}, \tag{16b}$$

in polar form, and similar equations in log-polar form for the outer mesh.

Rewriting and rearranging equations (16a) and (16b), using finite-difference quotient approximations to the derivatives, gives the following expressions, which are applicable to the inner region:

$$-\omega_{i-1j}^{k+1/2}\left[\frac{1}{r_j}-\frac{Re\,\Delta\theta}{4}\left(\frac{\partial\psi}{\partial r}\right)_{ij}^k\right]+\omega_{ij}^{k+1/2}\left[\frac{Re\,r_j\Delta\theta^2}{\Delta t}+\frac{2}{r_j}\right]$$

$$-\omega_{i+1j}^{k+1/2}\left[\frac{1}{r_j}+\frac{Re\,\Delta\theta}{4}\left(\frac{\partial\psi}{\partial r}\right)_{ij}^k\right]=\left\{\omega_{ij-1}^k\left[r_jP_1+\frac{L_3\overline{\Delta r_j}}{2}-\frac{Re\,L_3\overline{\Delta r_j}}{4}\left(\frac{\partial\psi}{\partial\theta}\right)_{ij}^k\right]\right.$$

$$+\omega_{ij}^k\left[\frac{Re\,r_j\overline{\Delta r_j^2}}{\Delta t}-\frac{Re\,L_2\overline{\Delta r_j}}{4}\left(\frac{\partial\psi}{\partial\theta}\right)_{ij}^k-r_jP_1P_3+\frac{L_2\overline{\Delta r_j}}{2}\right]$$

$$\left.+\omega_{ij+1}^k\left[r_jP_1P_2+\frac{L_1\overline{\Delta r_j}}{2}-\frac{Re\,L_1\overline{\Delta r_j}}{4}\left(\frac{\partial\psi}{\partial\theta}\right)_{ij}^k\right]\right\}\frac{\Delta\theta^2}{\overline{\Delta r_j^2}} \tag{17a}$$

and

$$-\omega_{ij-1}^{k+1}\left[P_1r_j+\frac{L_3\overline{\Delta r_j}}{2}-\frac{Re\,L_3\overline{\Delta r_j}}{4}\left(\frac{\partial\psi}{\partial\theta}\right)_{ij}^k\right]$$

$$+\omega_{ij}^{k+1}\left[\frac{Re\,r_j\overline{\Delta r_j^2}}{\Delta t}+\frac{Re\,L_2\overline{\Delta r_j}}{4}\left(\frac{\partial\psi}{\partial\theta}\right)_{ij}^k+P_1P_3r_j-\frac{L_2\overline{\Delta r_j}}{2}\right]$$

$$-\omega_{ij+1}^{k+1}\left[P_1P_2r_j+\frac{L_1\overline{\Delta r_j}}{2}-\frac{Re\,L_1\overline{\Delta r_j}}{4}\left(\frac{\partial\psi}{\partial\theta}\right)_{ij}^k\right]$$

$$=\left\{\omega_{i-1j}^{k+1/2}\left[\frac{1}{r_j}-\frac{Re\,\Delta\theta}{4}\left(\frac{\partial\psi}{\partial r}\right)_{ij}^k\right]+\omega_{ij}^{k+1/2}\left[\frac{Re\,r_j\Delta\theta^2}{\Delta t}-\frac{2}{r_j}\right]\right.$$

$$\left.+\omega_{i+1j}^{k+1/2}\left[\frac{1}{r_j}+\frac{Re\,\Delta\theta}{4}\left(\frac{\partial\psi}{\partial r}\right)_{ij}^k\right]\right\}\frac{\overline{\Delta r_j^2}}{\Delta\theta^2},\quad j=2,\dots,\text{NOJ}-1. \tag{17b}$$

Similar manipulations are performed on the log-polar form of the equations using central differencing approximations to the derivatives to give

$$-\omega_{i-1j}^{k+1/2}\left[1-\alpha\left(\frac{\partial\psi}{\partial Z}\right)_{ij}^{k}\right]+\omega_{ij}^{k+1/2}[2+\lambda E_z]-\omega_{i+1j}^{k+1/2}\left[1+\alpha\left(\frac{\partial\psi}{\partial Z}\right)_{ij}^{k}\right]=S^k, \tag{18a}$$

$$-\omega_{ij-1}^{k+1}\left[1+\beta\left(\frac{\partial\psi}{\partial\theta}\right)_{ij}^{k}\right]+\omega_{ij}^{k+1}\left[2+\frac{\lambda}{\mu}E_z\right]-\omega_{ij+1}^{k+1}\left[1-\beta\left(\frac{\partial\psi}{\partial\theta}\right)_{ij}^{k}\right]=S^{k+1} \tag{18b}$$

where

$$S^k=\mu\left\{\omega_{ij-1}^{k}\left[1+\beta\left(\frac{\partial\psi}{\partial\theta}\right)_{ij}^{k}\right]+\omega_{ij}^{k}\left[\frac{\lambda}{\mu}E_z-2\right]+\omega_{ij+1}^{k}\left[1-\beta\left(\frac{\partial\psi}{\partial\theta}\right)_{ij}^{k}\right]\right\}, \tag{18c}$$

$$S^{k+1}=\frac{1}{\mu}\left\{\omega_{i-1j}^{k+1/2}\left[1-\alpha\left(\frac{\partial\psi}{\partial Z}\right)_{ij}^{k}\right]+\omega_{ij}^{k+1/2}[\lambda E_z-2]+\omega_{i+1j}^{k+1/2}\left[1+\alpha\left(\frac{\partial\psi}{\partial Z}\right)_{ij}^{k}\right]\right\} \tag{18d}$$

and

$$\alpha=\frac{\Delta\theta\,Re}{4}, \qquad \beta=\frac{\Delta Z\,Re}{4}, \qquad \lambda=\frac{\Delta\theta^2}{\Delta t}Re, \qquad \mu=\frac{\Delta\theta^2}{\Delta Z^2}, \qquad \text{for} \quad j=\text{NOJ},\ldots,M-1.$$

Two linear systems of equations are obtained which are solved as follows. The first directional 'release' has the boundary condition $\omega_{N+1j}=\omega_{1j}$ on the $\theta=0$ axis. It is now possible to set up a tridiagonal matrix equation of the form

$$\begin{bmatrix} b_1 & -c_1 & & & & \\ -a_2 & b_2 & -c_2 & & & \\ & & \ddots & & & \\ & & -a_i & b_i & -c_i & \\ & & & & -a_N & b_N \end{bmatrix}\begin{bmatrix} \omega_{1j} \\ \omega_{2j} \\ \vdots \\ \omega_{ij} \\ \vdots \\ \omega_{Nj} \end{bmatrix}=\begin{bmatrix} K_1^* \\ K_2^* \\ \vdots \\ K_i^* \\ \vdots \\ K_N^* \end{bmatrix}. \tag{19}$$

It should be noted that lagged values of the vorticity terms ω_{Nj}^{k} and ω_{ij}, instead of unknown 'fictitious' vorticities $\omega_{Nj}^{k+1/2}$ and $\omega_{1j}^{k+1/2}$, are incorporated in the expressions for K_1^* and K_N^* in order to make the matrix tridiagonal.

The second directional 'release' requires the use of two boundary conditions for the vorticity. The vorticity is given by equation (6). At the cylinder surface the radius equals unity and the radial velocity is zero. Using a central differencing approximation the vorticity may be written

$$\omega_{i1}=\frac{r_2 V_{\theta_{i2}}-V_{\theta_{i1}}}{\Delta r_1}. \tag{20}$$

The outer boundary condition is

$$\omega_{iM}=\omega_{iM-1}. \tag{21}$$

Using these conditions, the following matrix equation can be constructed:

$$\begin{bmatrix} b_2 & -c_2 & & & & \\ -a_3 & b_3 & -c_3 & & & \\ & & \ddots & & & \\ & & -a_j & b_j & -c_j & \\ & & & -a_{M-1} & b_{M-1} \end{bmatrix}\begin{bmatrix} \omega_{i2} \\ \omega_{i3} \\ \vdots \\ \omega_{ij} \\ \vdots \\ \omega_{iM-1} \end{bmatrix}=\begin{bmatrix} K_2^* \\ K_3^* \\ \vdots \\ K_j^* \\ \vdots \\ K_{M-1}^* \end{bmatrix}$$

Using recursion formulae and Cholesky decomposition, equations (19) and (22) are solved to give the updated values of vorticity ω_{ij}^{k+1} throughout the mesh.

INITIAL AND BOUNDARY CONDITIONS

For the orbital flow case, the axis of the cylinder is considered to be stationary relative to the flow, as shown in Figure 4. The cylinder appears immersed in a forced vortex which has its centre some distance, R, from the cylinder and rotates with an angular velocity, Ω. The forced vortex is applied along with a theoretical doublet and real (potential) vortex representing the rotating cylinder to yield

$$\psi_{ij}^* = \left[-r\sin\theta\left(1 - \frac{1}{r^2}\right) - \frac{\pi}{2K_c}(r^2 + 2\ln r - 1) \right]_{ij},$$

where

$$R = \frac{U}{\Omega} \quad \text{and} \quad Kc = \frac{2\pi R}{D} = \frac{\pi R}{a}. \tag{23}$$

It should be noted that the expression for ψ_{ij}^* has been corrected in order to ensure that the surface stream function $\psi_{1j}^* = 0$. Owing to the presence of the forced vortex there is a uniform -initial vorticity

$$\omega_{ij} = \frac{2\pi}{Kc}. \tag{24}$$

This is derived by considering the rotationality at the outer boundary where the velocity components are known.

Various authors, including Dennis, Hudson and Smith,[20] Dennis and Chang[21] and Martinez,[10] used an Oseen vortex solution for the outer boundary vorticity for uniform flow past a cylinder. Dennis, Hudson and Smith obtained the following expression:

$$\omega_{iM} = \exp\left[\frac{Re}{4}(e^{Z_m} - e^{Z_{M-1}})(\cos\theta - 1) - \tfrac{1}{2}(Z_M - Z_{M-1})\right]\omega_{iM-1}. \tag{25}$$

This equation is cumbersome and is limited to low Reynolds numbers and small grid sizes. Otherwise, unmanageably large numbers are generated within the computation process. A simple alternative which involves assuming a uniform vorticity gradient $\partial\omega/\partial Z = 0$ at the outer boundary gives equation (21). This was found to be quite adequate for both uniform and orbital flow problems.

The outer boundary stream function is assumed equal to the potential flow stream function.
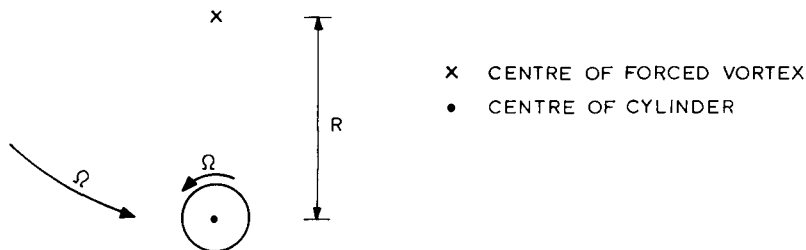
Figure 4. Orbital flow representation

Thus

$$\psi_{iM} = \psi_{iM}^{*}. \tag{26}$$

The radial and angular velocity components at the outer boundary are given by

$$V_{\theta_{iM}} = -E_z^{-1/2} \frac{\psi_{iM} - \psi_{iM-1}}{\Delta Z} \tag{27}$$

and

$$V_{r_{iM}} = \frac{\psi_{i+1M} - \psi_{i-1M}}{2\,\Delta\theta E_z^{1/2}}. \tag{28}$$

The surface boundary vorticity is given by equation (20). In all cases the surface boundary stream function and radial velocity were fixed to give

$$\psi_{i1} = V_{r_{i1}} = 0. \tag{29}$$

The surface angular velocity of the cylinder must be the same as the angular velocity of the forced vortex in the orbital flow case. Thus

$$V_{\theta_{i1}} = \Omega, \quad \text{where} \quad \Omega = \pi/Kc. \tag{30}$$

CALCULATION OF SURFACE PRESSURE DISTRIBUTION

A reference value of surface pressure P_{11}, close to the front of the cylinder, was fixed at $1/2$ for the orbital flow cases considered.

After some algebraic manipulation the angular components of the Navier–Stokes equations can be reduced to the following expression:

$$\frac{\partial P}{\partial \theta} = \frac{2}{Re} \frac{\partial \omega}{\partial r} + \rho \frac{\pi}{Kc} \cos \theta. \tag{31}$$

This is rewritten using finite-difference approximations to give

$$P_{i+1} = P_i + \frac{\Delta\theta}{Re} \left[\left. \frac{\partial \omega}{\partial r} \right|_{i+1} + \left. \frac{\partial \omega}{\partial r} \right|_{i} \right] + \rho \frac{\pi}{Kc} \cos \theta_{i+1/2} \, \Delta\theta. \tag{32}$$

Using a third-order Lagrangian polynomial to fit the vorticity gradients it is possible to obtain

$$\begin{aligned}
\left. \frac{\partial \omega}{\partial r} \right|_i = 5\sqrt{Re} \Bigg\{ & \frac{(K+2)(K^2+2K+2)(K^3+2K^2+2K+2)}{(K+1)^4(1+K+K^2)} [\omega_{i2} - \omega_{i1}] \\
& - \frac{(K^2+2K+2)(K^3+2K^2+2K+2)}{K^3(K+1)^4} [\omega_{i3} - \omega_{i2}] \\
& + \frac{(K+2)(K^3+2K^2+2K+2)}{K^5(K+1)^4} [\omega_{i4} - \omega_{i3}] \\
& - \frac{(K+2)(K^2+2K+2)}{K^6(K+1)^4(K^2+K+1)} [\omega_{i5} - \omega_{i4}] \Bigg\}
\end{aligned} \tag{33a}$$

and

$$
\begin{aligned}
\left.\frac{\partial \omega}{\partial r}\right|_{i+1} = 5\sqrt{Re}\Bigg\{ &\frac{(K+2)(K^2+2K+2)(K^3+2K^2+2K+2)}{(K+1)^4(1+K+K^2)}[\omega_{i+1\,2}-\omega_{i+1\,1}] \\
&-\frac{(K^2+2K+2)(K^3+2K^2+2K+2)}{K^3(K+1)^4}[\omega_{i+1\,3}-\omega_{i+1\,2}] \\
&+\frac{(K+2)(K^3+2K^2+2K+2)}{K^5(K+1)^4}[\omega_{i+1\,4}-\omega_{i+1\,3}] \\
&-\frac{(K+2)(K^2+2K+2)}{K^6(K+1)^4(K^2+K+1)}[\omega_{i+1\,5}-\omega_{i+1\,4}]\Bigg\}.
\end{aligned} \tag{33b}
$$

The surface pressures are now computed by stepping numerically around the cylinder in an anticlockwise direction, from the reference value, P_{11}. The resulting pressures are expressed as a coefficient C_{pi1} given by

$$
C_{pi1} = 2P_{ij}. \tag{34}
$$

Using this method the surface pressure shows a mismatch at the ends of the closed loop. Thoman[22] suggested that the degree of mismatch gives an estimate of the numerical error and found that mismatches as much as 5 per cent of the total span sometimes occurred in his computations. In the work presented in this paper, the closure mismatch was largest at earliest time stages when the vorticity gradients close to the surface were largest.

It should be noted that a more exact approach for the evaluation of surface pressures has been developed by Collins and Dennis[23] and Badr and Dennis.[24] They used Fourier analysis to reduce the governing vorticity-transport and stream-function equations to sets of time-dependent equations which are solved numerically. Their method ensures that the fluid pressure is exactly a periodic function of period 2π and that the circulation round a sufficiently large contour remains zero.

DRAG AND LIFT COEFFICIENTS

The drag and lift coefficients, C_d and C_L, respectively, are obtained by performing the following integrations using a Simpson's rule numerical approximation:

$$
C_d = -\int_0^{2\pi} P\cos\theta\,\mathrm{d}\theta - \frac{2}{Re}\int_0^{2\pi}\omega\sin\theta\,\mathrm{d}\theta \tag{35}
$$

and

$$
C_L = -\int_0^{2\pi} P\sin\theta\,\mathrm{d}\theta + \frac{2}{Re}\int_0^{2\pi}\omega\cos\theta\,\mathrm{d}\theta. \tag{36}
$$

RESULTS FOR UNIFORM FLOW PAST STATIONARY AND ROTATING CYLINDERS

Both the regular and hybrid meshes were used to simulate uniform flow past a stationary cylinder. Three Reynolds numbers were investigated in detail, namely 100, 200 and 1000. Figure 5 charts the development of the drag and lift coefficients determined using the hybrid mesh. The drag coefficients have higher values than those computed using the coarse regular grid discussed by

Thoman and Szewczyk.[7] Stream-function, vorticity and velocity distributions and velocity profiles through the boundary layers were also computed. It was observed that the hybrid mesh scheme gives a valuable insight into the behaviour within the boundary layers, unlike the rough grid. Also, higher Reynolds numbers can be investigated. In general, the results agree with those obtained by Thoman and Szewczyk.

Thoman and Szewczyk[7] also examined several cases of uniform flow past a rotating cylinder. They chose various speeds of rotation greater than the incident velocity in order to study the Magnus effect. Although one comparable case is presented here, the rest are concerned with cylinders rotating at a slower speed than that of the incident flow. In orbital flow the surface of the cylinder rotates at a speed given by π/Kc, where Kc is the Keulegan–Carpenter number. For example, when Kc equals 12 or 24 the surface velocity is 0.2618 or 0.1309, respectively.

Recently published experimental work by Coutanceau and Ménard[25] and numerical simulations by Badr and Dennis[24] have examined the near wake development behind an impulsively started rotating cylinder under translation in uniform flow. In their complementary investigations, the relative speeds of rotation varied from 0 to 3·25 for $Re = 200$, 500 and 1000. In particular, Coutanceau and Ménard present flow visualizations for $Re = 200$ and relative velocities of 0·28 and 2·07. These visualizations agree closely with the numerical results obtained by Borthwick[2] for $Re = 200$ and relative velocities of 0·25 and 2.

Figure 6 shows the development of drag and lift coefficients with time for speeds of rotation of 0·1, 0·25 and 2 at a Reynolds number of 200. For the two lower speeds, the drag coefficient attains a similar mean value, close to 2·0, with a uniform sinusoidal component indicating vortex shedding. The onset of vortex shedding occurs earlier at a relative speed of 0·25 than at a speed of 0·1. However, the drag coefficient obtained for the largest relative speed of 2 shows that any initial vortex-induced oscillations die out, and the drag coefficient settles to a constant value of almost 1·2. Similar effects are noticeable in the plots of lift coefficient with time.

Comparisons of computed and measured mean lift and drag coefficients are given in Figure 7. There is a large scatter in the measured lift coefficients, owing to the influence of the aspect ratio and end conditions as described by Swanson.[26] Thoman[22] calculated a higher value of drag and a lower value of lift than the author for the largest velocity ratio of 2. The differences are due to the use of the ADI method here instead of the upwind differencing approach used by Thoman.

The mean lift coefficients presented here lie between those expected for an ideal fluid and those measured experimentally by Thom[27] for a Reynolds number range of $5.3–8.8 \times 10^3$. Further consideration of Figure 7 indicates that for low velocity ratios an increase in Reynolds number from 200 to 1000 causes a slight reduction in both drag and mean lift coefficients.

The velocity profiles through the boundary layers do agree reasonably with those computed by Thoman[22] and measured experimentally by Swanson.[26] This is illustrated in Figure 8.

Obviously, increases in the relative velocity below a certain value bring forward the onset of vortex shedding and increase the magnitude of the mean lift coefficient. However, there exists a transition point at which the rotational speed of the cylinder becomes sufficient to dominate the flow and so suppress any vortex shedding. Figures 9 and 10 demonstrate the tremendous differences in flow patterns obtained by varying the rotational speed from 0·25 to 2·0. For orbital flow, this may be comparable to decreasing the Keulegan–Carpenter number from about 12 to 1·5. In other words, for an orbit small enough relative to the cylinder, vortex shedding could be effectively damped and a Magnus-type increase in lift experienced by the cylinder.

One difficulty, encountered when considering rotating cylinders, is that the separation points, if any, cannot be readily determined from the surface vorticity distribution. Sears and Telionis[28] suggest that in non-steady flows separation occurs when the shearing stress at an internal stagnation point vanishes. Thus for separation

A. BORTHWICK
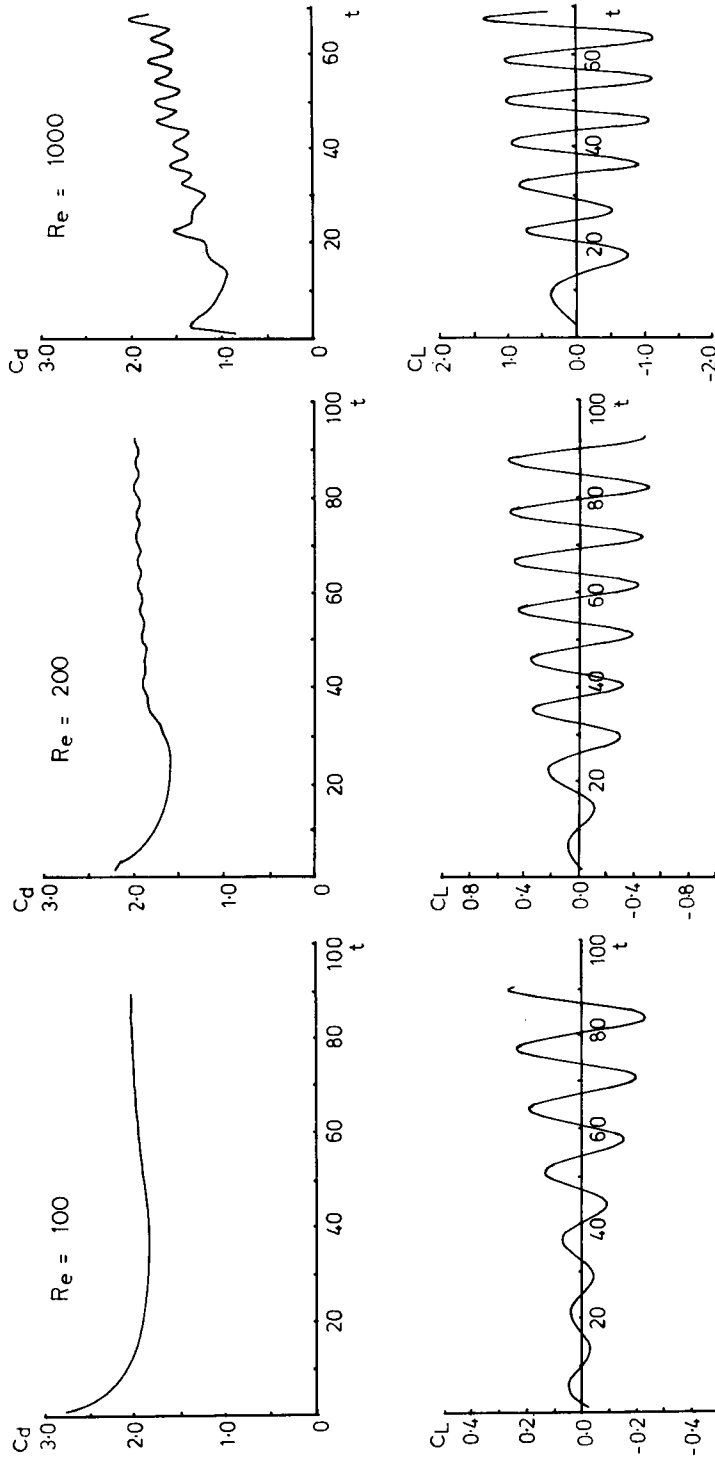
Figure 5. Drag and lift coefficients: $Re = 100, 200$ and 1000
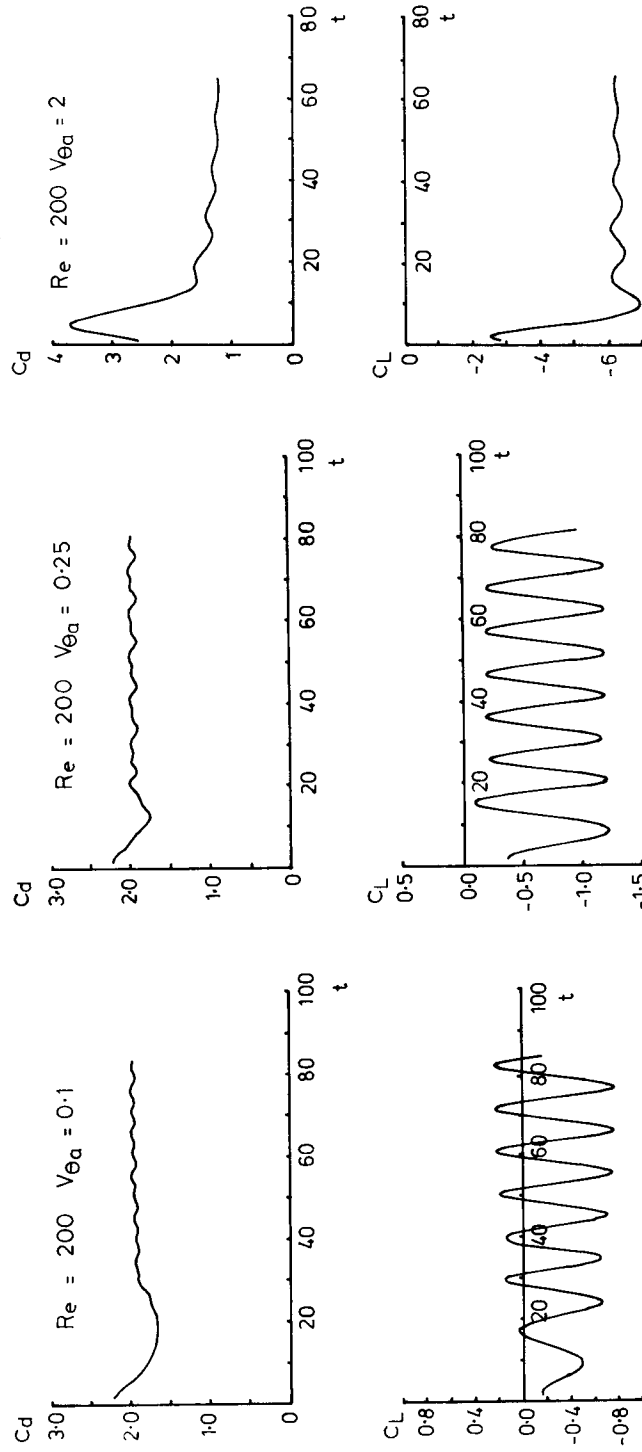
Figure 6. Drag and lift coefficients: $Re = 200$, $V_{\theta_1} = 0.1$, 0.25 and 2
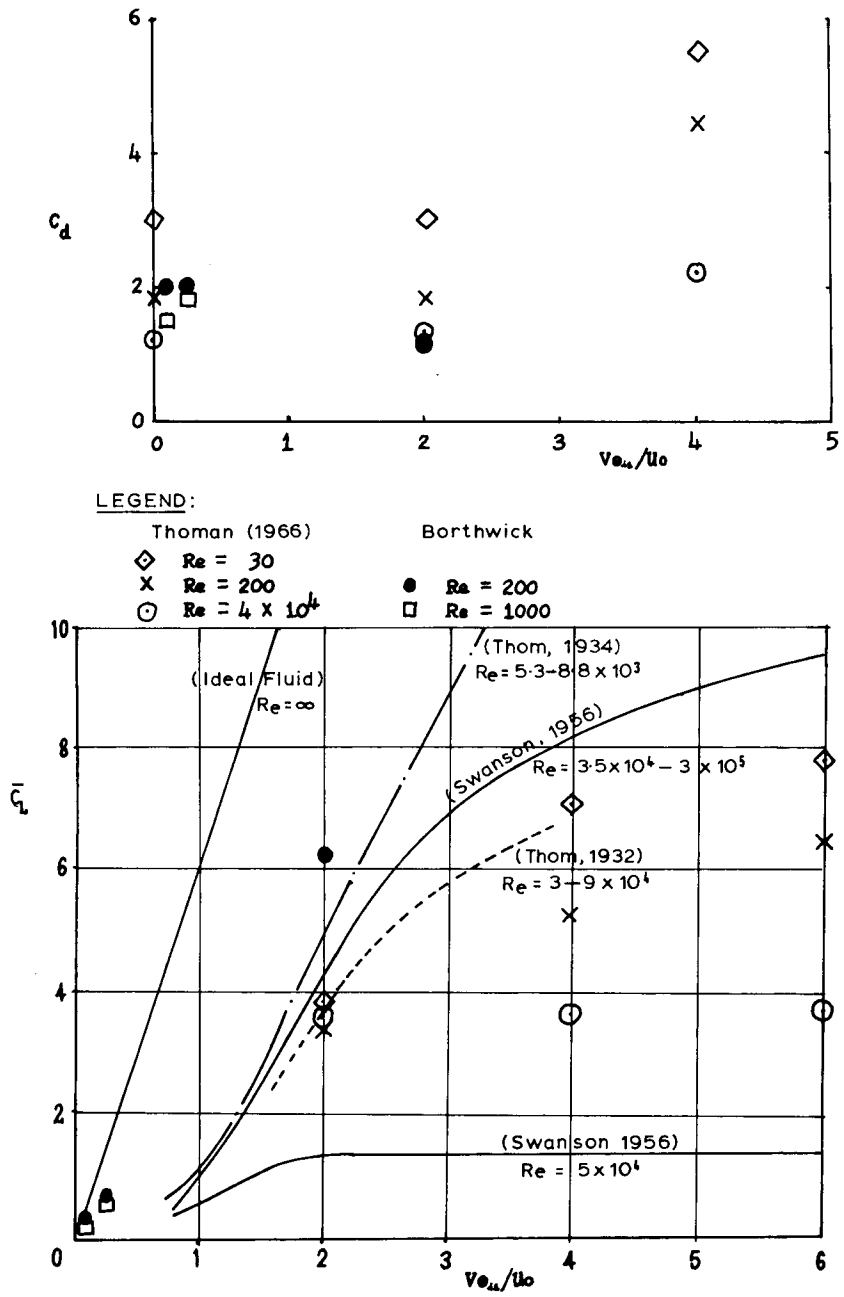
Figure 7. Comparison of computed and measured lift and drag coefficients

$$V_\theta = 0 \quad \text{and} \quad \frac{\partial V_\theta}{\partial r} = 0 \quad \text{in the interior.} \tag{37}$$

This condition is known as the Moore–Rott–Sears criterion,[12] and is applied here in order to estimate accurately the position of the separation points with the use of the velocity profiles
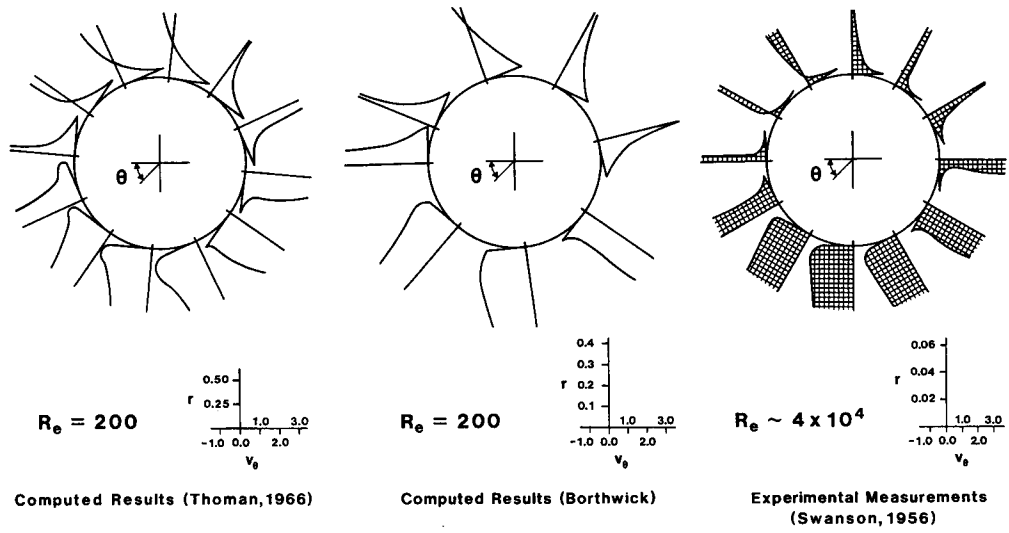
Figure 8. Comparison of computed and measured tangential velocity profiles through the boundary layer for a relative velocity of 2
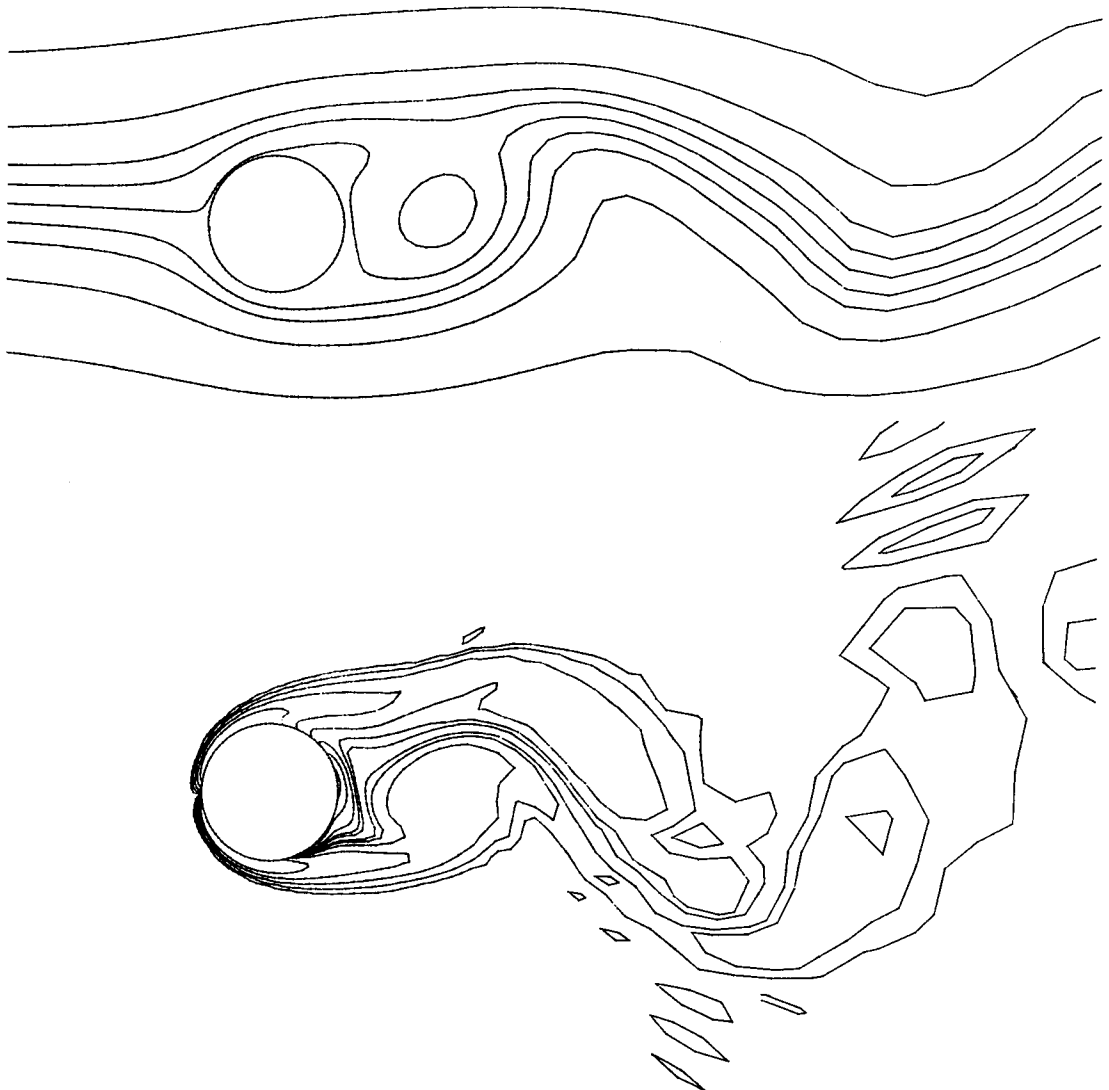
Figure 9. Stream-function and vorticity contours: $Re = 200$, $V_{\theta_{i1}} = 0.25$, $t = 63.665$
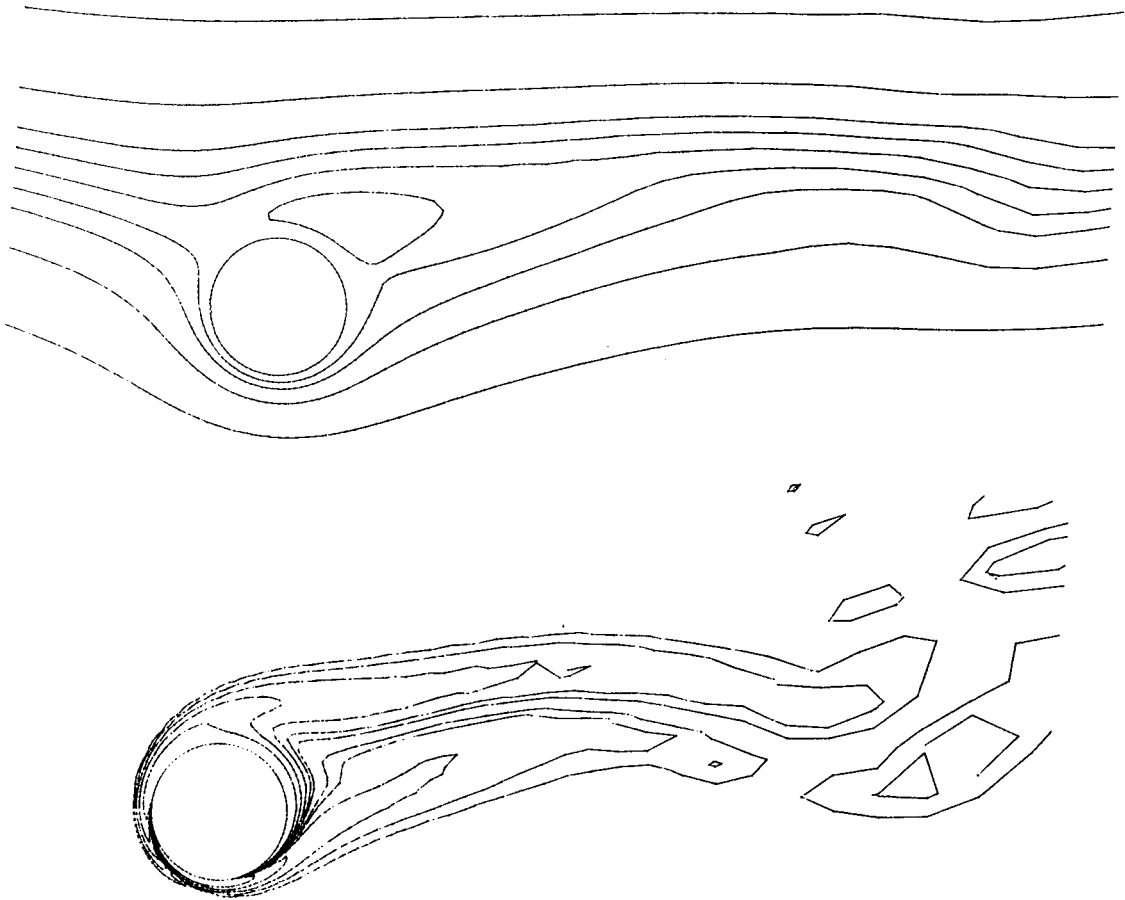
Figure 10. Stream-function and vorticity contours: $Re = 200$, $V_{\theta_{11}} = 2$, $t = 48\cdot437$

through the boundary layers. For example, on studying the plot given in Figure 11, at a time of 58·656, for a Reynolds number of 1000 and speed of rotation of 0·25, the surface vorticity passes through zero at 91°. However, consideration of the velocity profiles through the boundary layer, shown in Figure 12, demonstrates that separation actually occurs at 114°. Examination of the overall velocity distribution behind the cylinder, in Figure 13, confirms this.

HYBRID MESH RESULTS FOR ORBITAL FLOW PAST A CYLINDER

An orbital flow with a Keulegan–Carpenter number of 12 was examined for Reynolds numbers of 100 and 1000. The number of numerical investigations carried out was restricted by the very large amount of computer resources required. More than one hundred seconds of time from a CDC7600S machine was required in order to compute each unit of dimensionless time for the flow.

Plots of drag and lift coefficients with time for a Keulegan–Carpenter number of 12 and Reynolds number 100 are given in Figure 14. The graphs cover several complete revolutions where the period is equal to $2Kc$. These plots show that there is a large fluctuation in the forces just after the completion of each cycle for the first few revolutions. The sudden drops experienced
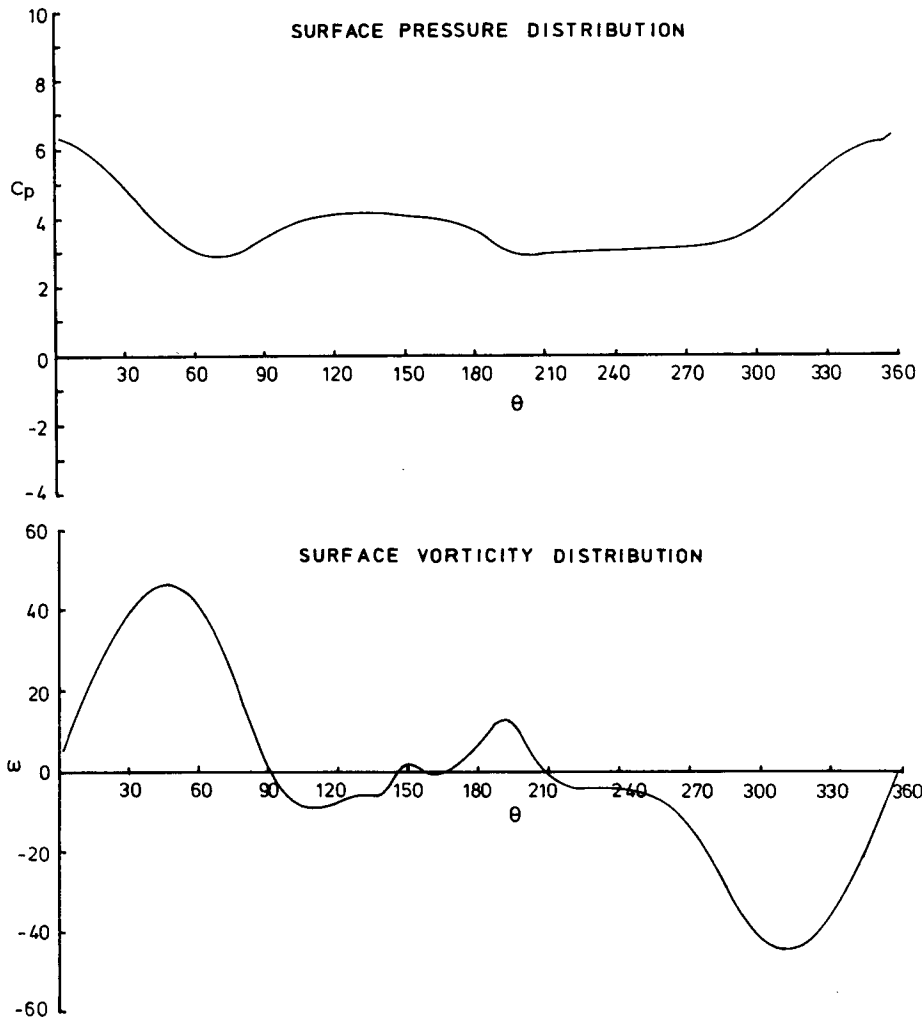
Figure 11. Surface pressure and vorticity distribution: $Re = 1000$, $V_{0_{i_1}} = 0{\cdot}25$, $t = 58{\cdot}656$
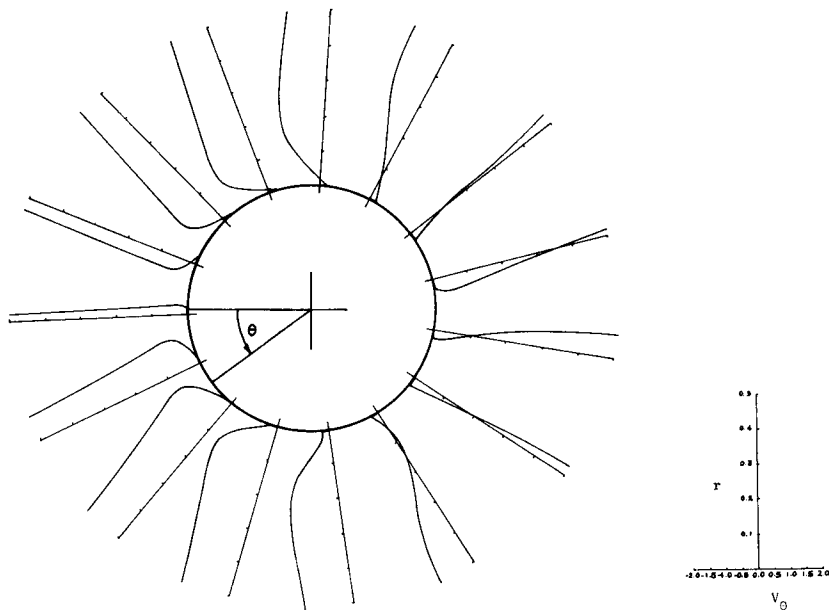
Figure 12. Tangential profiles: $Re = 1000$, $V_{0_{i_1}} = 0{\cdot}25$, $t = 58{\cdot}656$
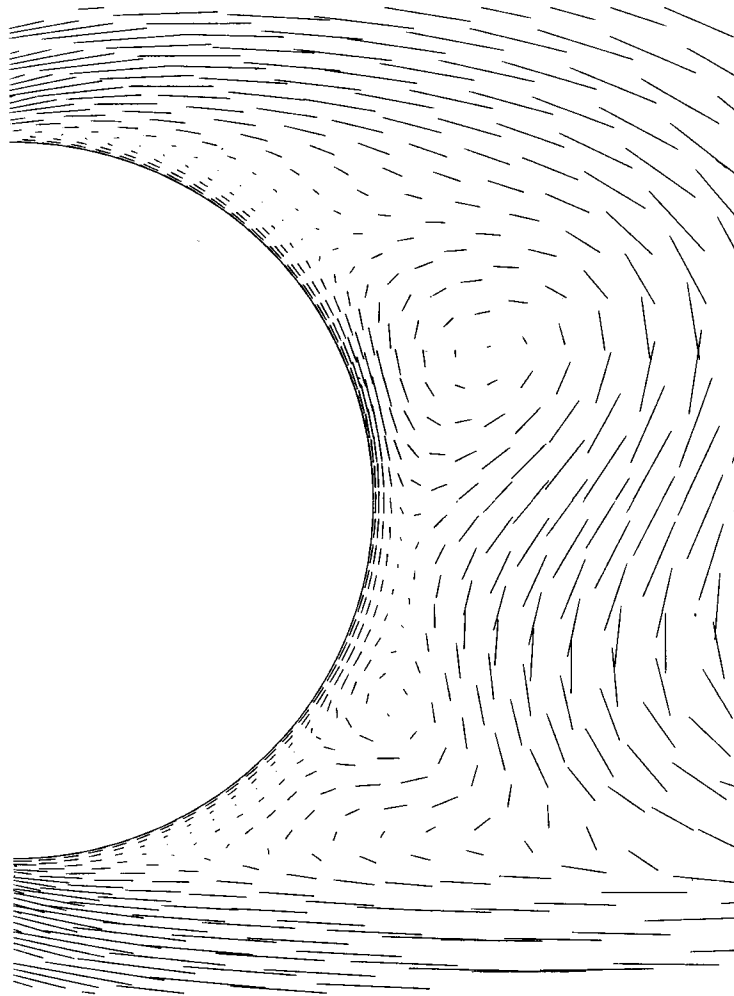
Figure 13. Velocity distribution behind the cylinder: $Re = 1000$, $V_{\theta_{11}} = 0.25$, $t = 58.656$

by the drag coefficient correspond to residual disturbances in the wake, caused by the impulsive start, passing around the orbit and colliding with the cylinder after each cycle.

This effect dies out eventually. The fluctuating forces experienced by the cylinder then become almost entirely dependent on the vortex shedding process and the relative positions and strengths of vortices left in the flow. With time, the number of vortices residing in the proximity of the orbit is sufficient to distort the early circular pattern. The orbit itself does not disappear, but alters progressively from one configuration to another as vortices detach from the cylinder, move around the orbit and gradually spiral outward, as can be seen in Figures 19 and 20.

Immediately after the impulsive start, the high values of surface vorticity generated swamp the forced vortex that represents the orbit. At a time close to a value of 1·5, a vortex reappears behind the cylinder and centres itself above the cylinder by a time of 10·5. Its position corresponds to that of the forced vortex representing the flow orbit, as shown in Figure 15. It should be noted that the centre of the orbit is assumed to be directly above the centre of the cylinder.

The difference in velocity on the surface of the cylinder at points nearest and furthest from

DRAG COEFFICIENT
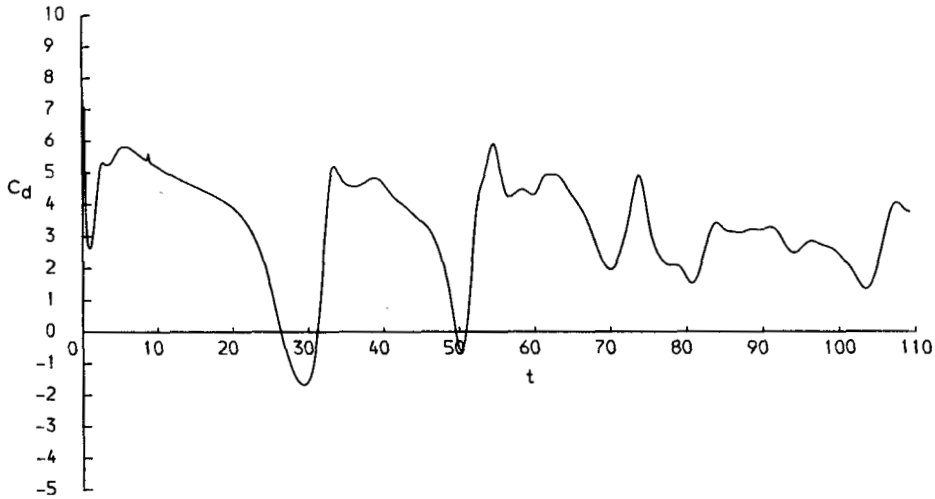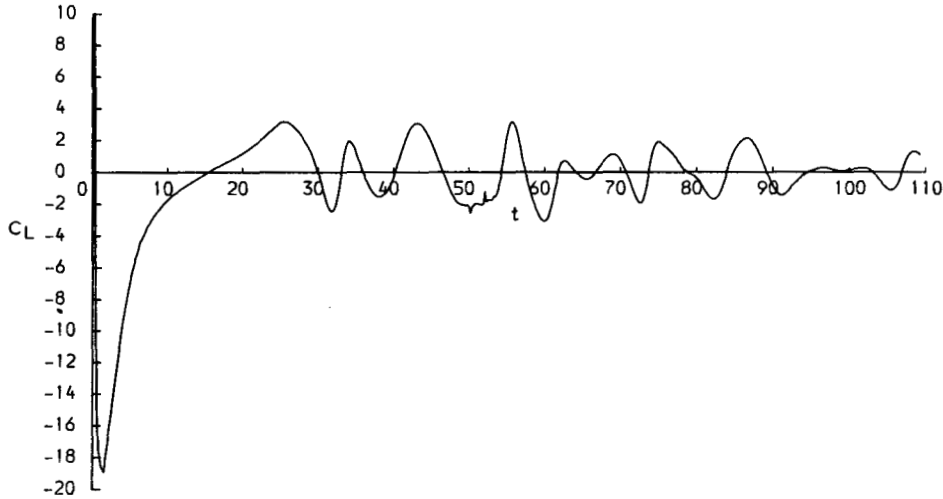
LIFT COEFFICIENT

Figure 14. Drag and lift coefficients: $Re = 100$, $Kc = 12$

the centre of the forced vortex (which represents the incident orbital flow) causes an anticlockwise vorticity flux around the cylinder. Thus the wake produced is asymmetric. Greater amounts of vorticity are generated on the lower part of the cylinder furthest from the centre of the orbit and at a higher velocity than the upper part. Therefore a curved wake begins to form behind the cylinder. The vorticity at the lower part of this wake, where the orbital velocity is greatest, rolls up, and by a time $t = 8$, a vortex detaches. This nearly circular anticlockwise vortex moves

around the complete orbit and by time $t = 25$ collides with the lower front surface of the cylinder, causing a sudden reduction in the drag coefficient. As the vortex collides with the cylinder it distorts to an almost flat ellipsoid and pulls some of the upper part of the cylinder wake over the top of the cylinder. This is illustrated in Figure 16.

Meanwhile, by time $t = 31$, a second vortex detaches from the lower part of the wake behind the cylinder and starts moving around the orbit. The first vortex, which has lost a significant amount of strength owing to the assimilation of part of its circulation into the wake as it passed below the cylinder, becomes absorbed into a vortex growing in the upper part of the wake behind the cylinder.

The portion of the wake that was pulled over the top of the cylinder detaches and flows under the cylinder as a vortex. It then spirals outwards, following the path of the orbit, rapidly losing strength. The wake establishes itself behind the cylinder again, at time $t = 35 \cdot 404$. The position of the second vortex lies almost at the centre of the orbit, which is still fairly circular.

As the second vortex continues to move round, a fourth vortex sheds from the upper part of the wake at time $t = 42$. The second vortex starts to collide with the surface of the cylinder at time $t = 45$, while a fifth vortex is shedding from the lower part of the wake behind the cylinder. The collision of the rather weak second vortex is followed by the impact of the larger fourth vortex at a time $t = 53$. This causes a similar effect to that experienced during the first collision, where part of the upper wake is pulled over the top of the cylinder and detaches as a small vortex. The process is illustrated in Figure 17 which shows the stream-function and vorticity contours at times of $48 \cdot 802$, $52 \cdot 629$ and $56 \cdot 457$.

The approach and impact of the vortex on the surface of the cylinder causes large relative movement of the surface vorticity with corresponding dramatic changes in pressure. This is shown in Figure 18, where positive values of pressure are found at an angle of $240°$ approximately behind the cylinder, at a time of $48 \cdot 80$. This positive pressure increases in magnitude (as do the negative values) and moves to a position of $320°$ at a time of $52 \cdot 63$. The movement of positive pressure towards the front of the cylinder is complete by $t = 56 \cdot 46$ when the pressure and vorticity plots settle to profiles fairly typical of steady flow.

With time more vortices detach and move around the orbit; the wake having formed again behind the cylinder. There seems to be sufficient residual vorticity left in the orbital path for these vortices to be deflected outward and no longer impinge on the front of the cylinder. Typical flow patterns are shown in Figures 19 and 20. The flow can be considered to have settled somewhat after three revolutions.

The wake behind the cylinder becomes quite asymmetric, with the upper part curling around and growing in the direction of the orbital path until its extremities break off and diffuse into the flow. The lower part of the wake continues to shed vortices, which join the others circling outwards around the orbit and eventually are diffused by viscosity. Typical stream-function and vorticity plots are given in Figure 21 which shows the flow pattern at times $t = 94 \cdot 735$, $99 \cdot 519$ and $104 \cdot 304$ after approximately four cycles. The surface pressure and vorticity plots have a more or less constant form, as indicated in Figure 22, which gives the results at a time $t = 99 \cdot 52$. The same applies to the velocity profiles taken through the boundary layers, presented in Figure 23. The profiles remain similar for each case and indicate that separation is occurring at $160°$ and $240°$ approximately. This is confirmed by inspection of the contour plots. Obviously, discrete vortex simulations of orbital flow must take into account the movement of the separation points; otherwise, the model will produce incorrect results.
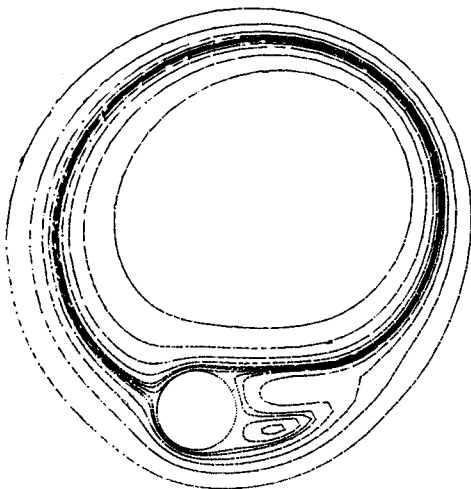
The second case study deals with a flow of Reynolds number 1000 and Keulegan–Carpenter number 12. The drag and lift coefficients are given in Figure 24. They display rapid fluctuations with time. The most rapid variations occur at times of 0 to 10 and 88 to 98 when a time step
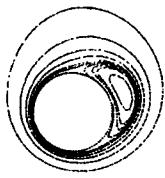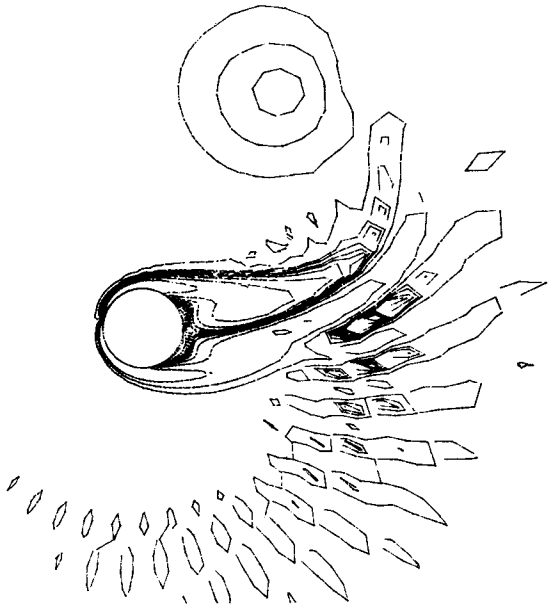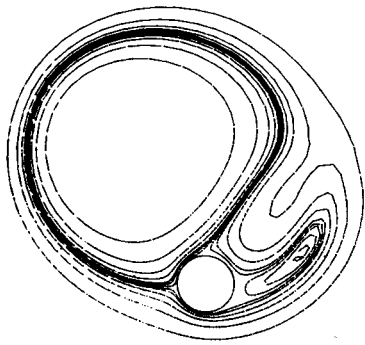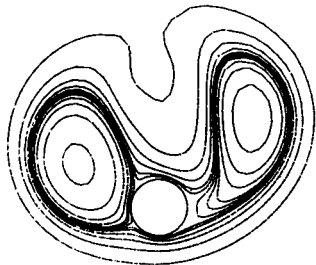
$t = 1.529$
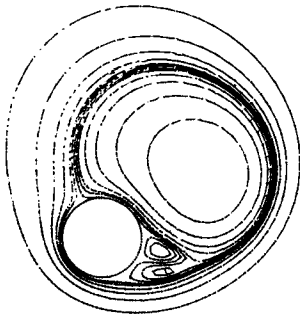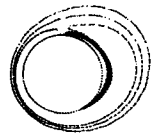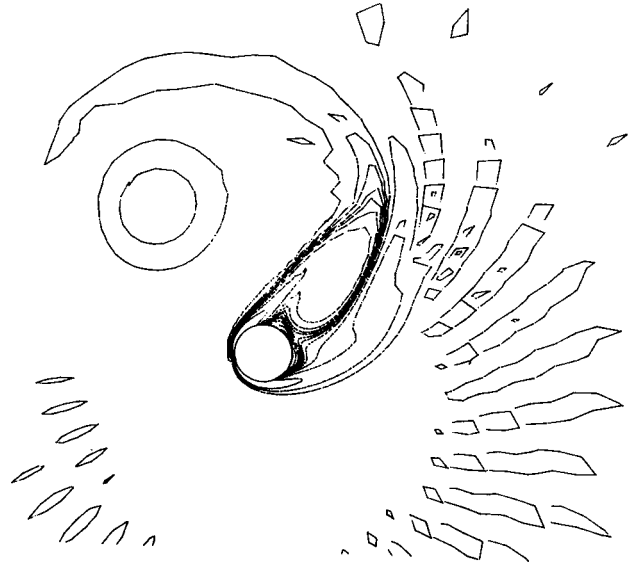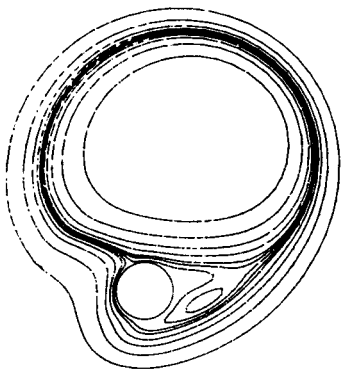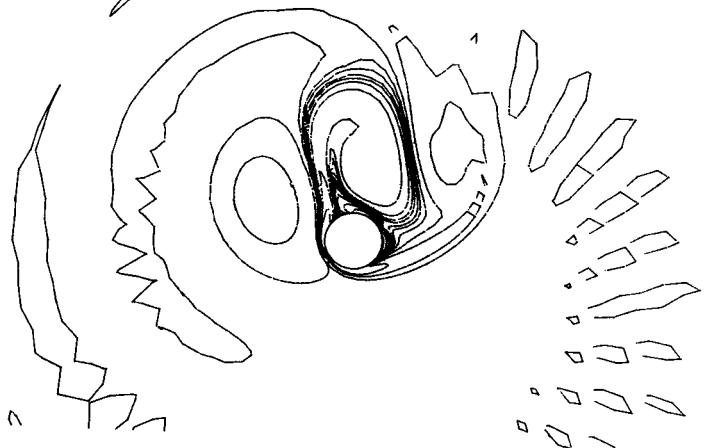
$t = 4.591$

$t = 10.524$

Figure 15. Stream-function and vorticity contours: $Re = 100$, $Kc = 12$, $t = 1.529$, 4.591 and 10.524
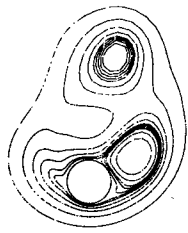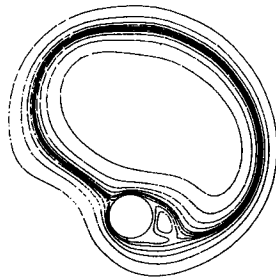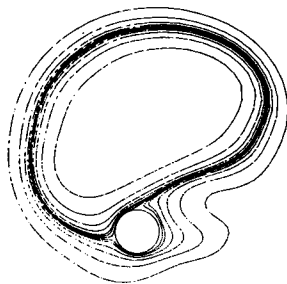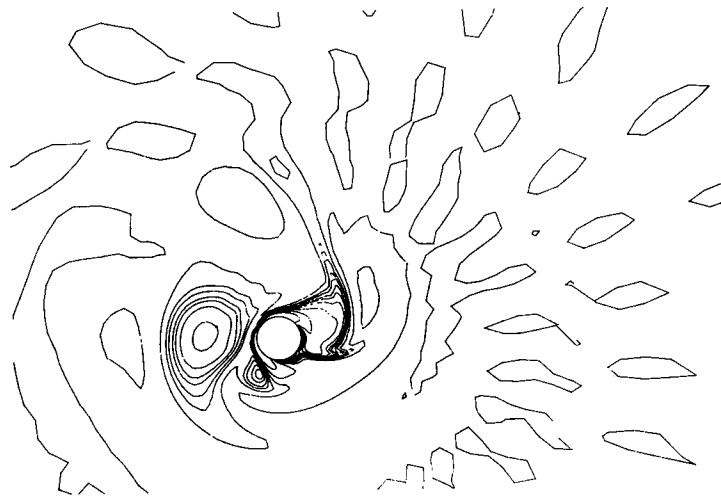
$t = 20.094$

$t = 25.835$

$t = 31.576$

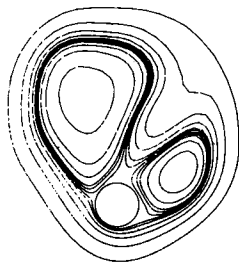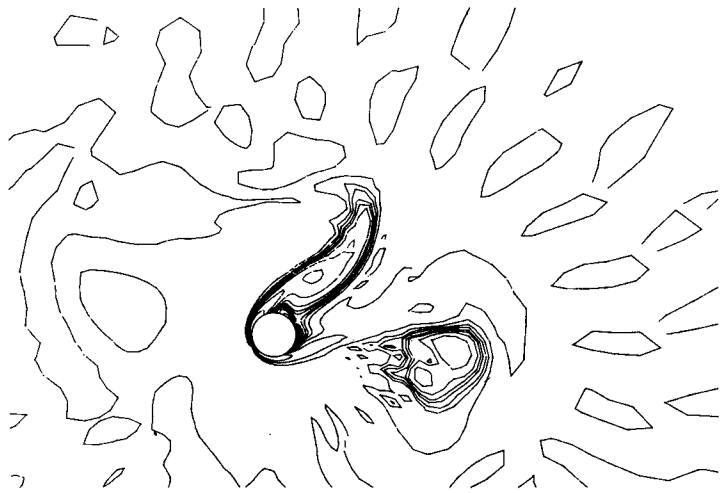Figure 16. Stream-function and vorticity contours: $Re = 100$, $Kc = 12$, $t = 20.094$, 25.835 and 31.576

$t = 48 \cdot 802$

$t = 52 \cdot 629$

$t = 56 \cdot 457$

Figure 17. Stream-function and vorticity contours: $Re = 100$, $Kc = 12$, $t = 48 \cdot 802$, $52 \cdot 629$ and $56 \cdot 457$
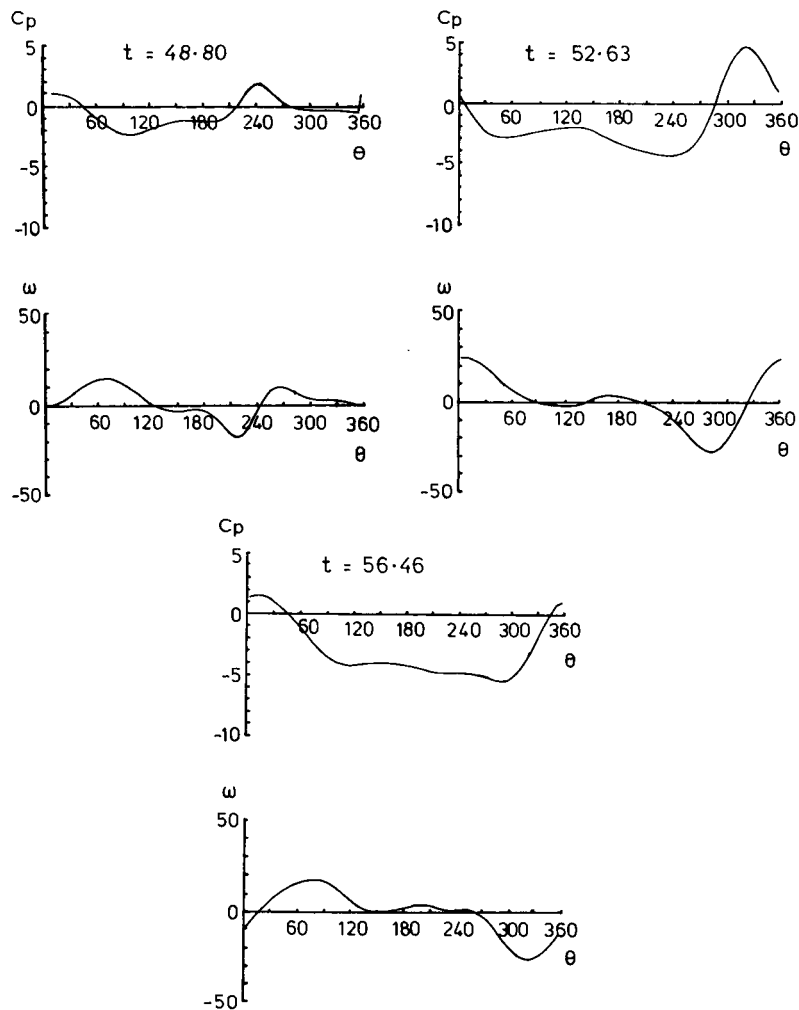
Figure 18. Surface pressure and vorticity distributions: $Re = 100$, $Kc = 12$, $t = 48 \cdot 802$, 52.629 and $56 \cdot 457$

satisfying the stability criterion was used. An increase in the time step by a factor of 5 was used for the rest of the computation, and appears to filter out the highest frequency components. The cause of these rapid fluctuations is not known. However, regular vortex shedding is evident throughout the development of the flow. The sinusoidal nature of the drag and lift shows this.

An initial sequence of events similar to those described previously occurs. At the earliest stages, surface vorticity on the impulsively started cylinder dominates the flow. Then a vortex detaches from behind the cylinder and establishes the flow pattern of the orbit. The vortex shedding process is much more rapid in this case, owing to the higher Strouhal number to be expected for the higher Reynolds number (in this range). This leads to large numbers of vortices circling the orbit and distorting its shape a great deal, as can be seen in Figure 25 which also shows the unsteady nature of the flow as it impinges on the cylinder. These vortices gradually spiral outward as others detach from the cylinder and join the orbital path. Secondary vortices are evident close to the surface of the cylinder.
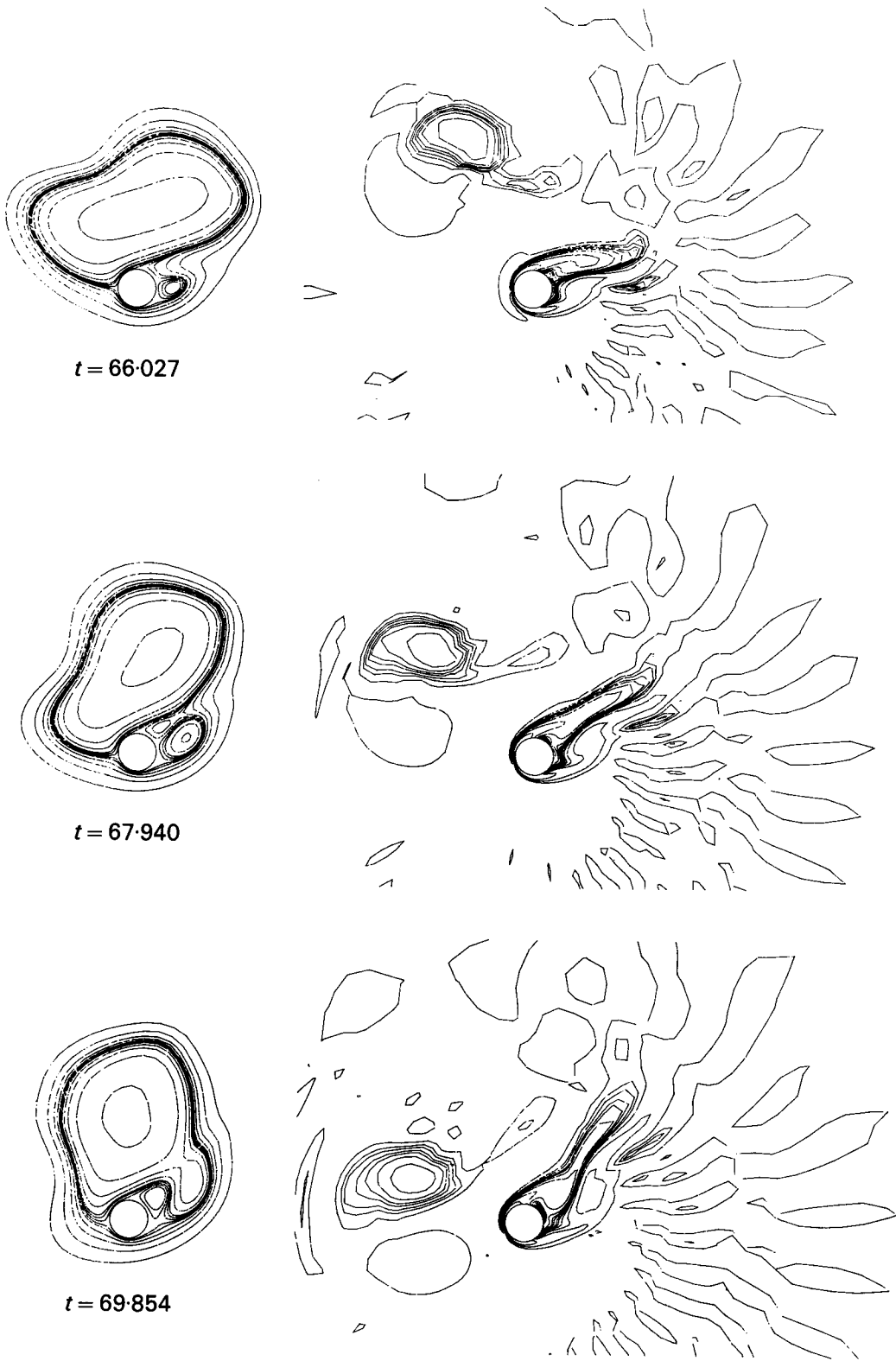
Figure 19. Stream-function and vorticity contours: $Re = 100$, $Kc = 12$, $t = 66 \cdot 027$, $67 \cdot 940$ and $69 \cdot 854$
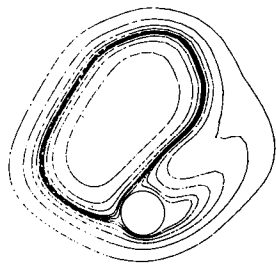
$t = 77 \cdot 510$

$t = 79 \cdot 424$
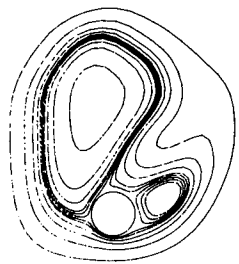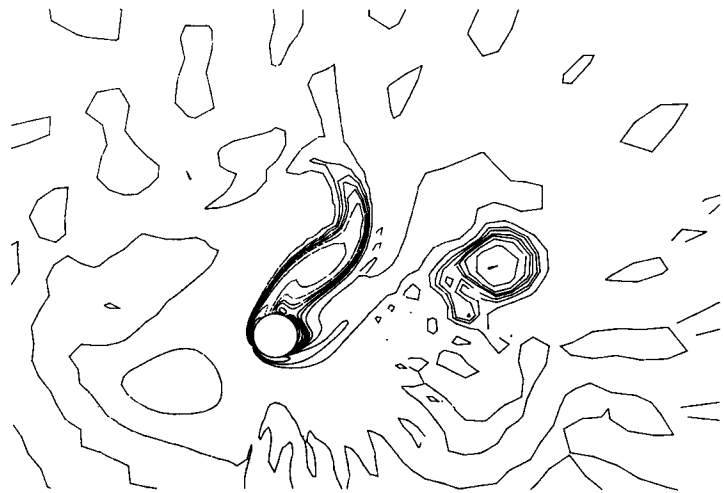
$t = 81 \cdot 337$

Figure 20. Stream function and vorticity contours: $Re = 100$, $Kc = 12$, $t = 77 \cdot 510$, $79 \cdot 424$ and $81 \cdot 337$
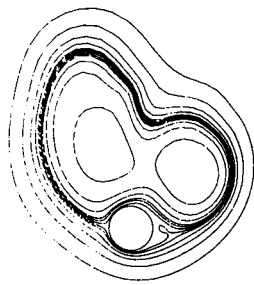
$t = 94 \cdot 735$
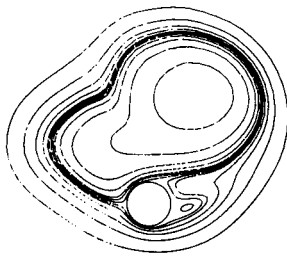
$t = 99 \cdot 519$
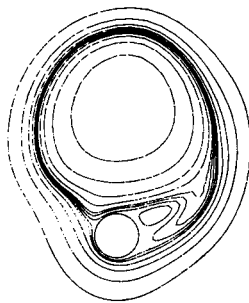
$t = 104 \cdot 304$
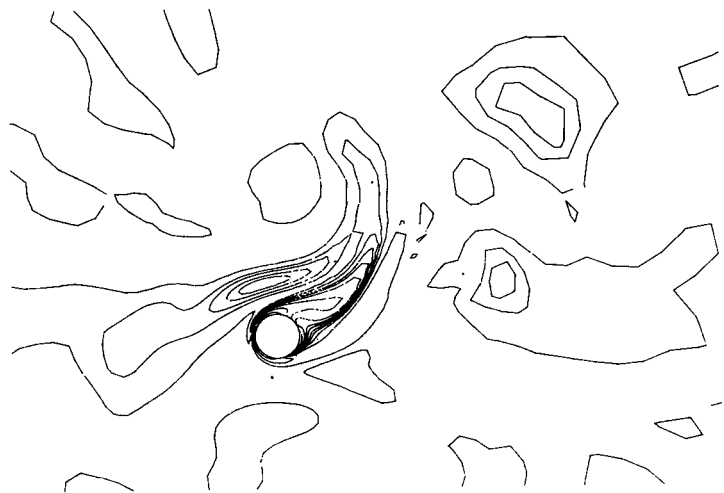
Figure 21. Stream function and vorticity contours: $Re = 100$, $Kc = 12$, $t = 94 \cdot 735$, $99 \cdot 519$ and $104 \cdot 304$
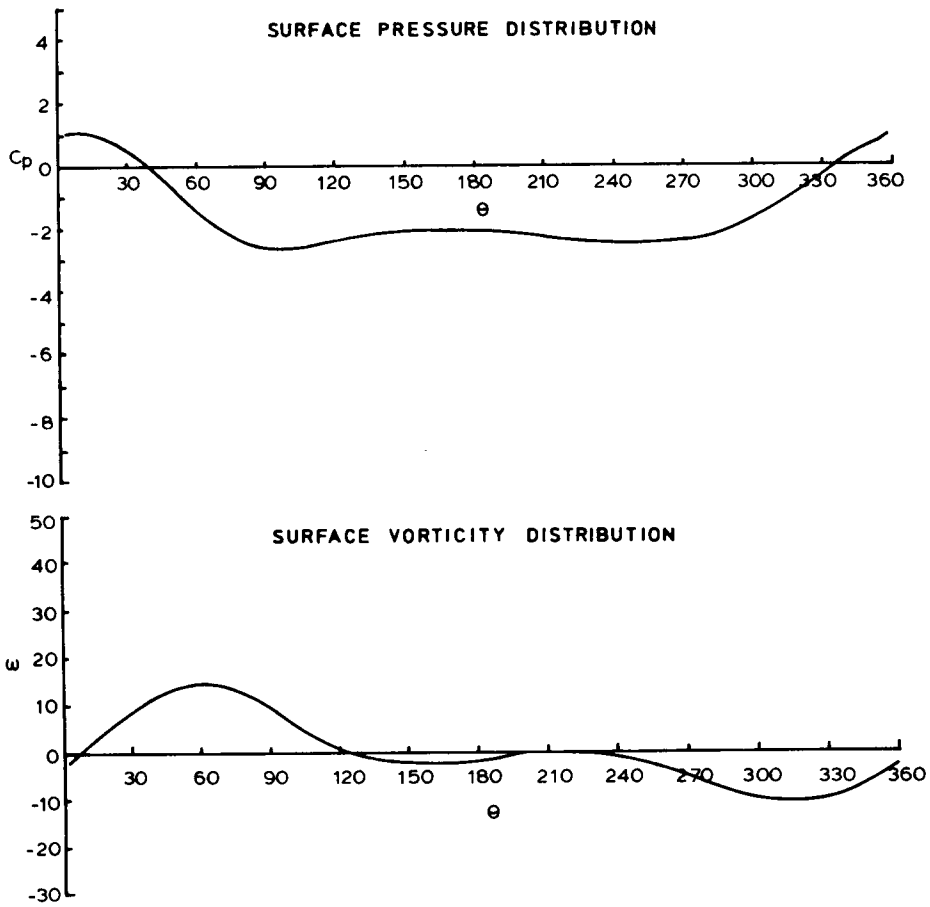
Figure 22. Surface pressure and vorticity distributions: $Re = 100$, $Kc = 12$, $t = 99 \cdot 519$
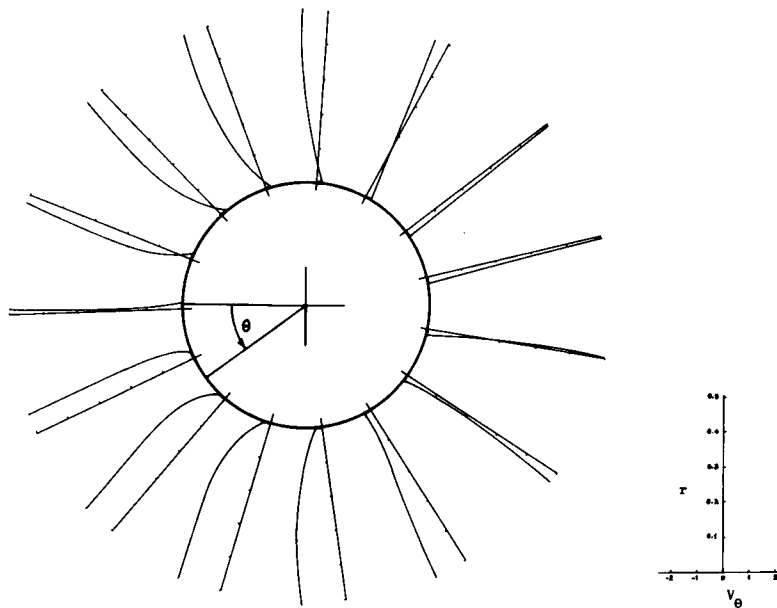
Figure 23. Tangential velocity profiles: $Re = 100$, $Kc = 12$, $t = 99 \cdot 519$
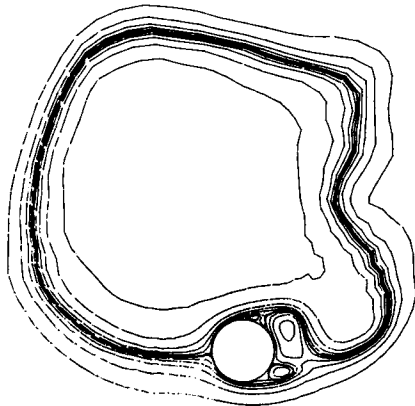
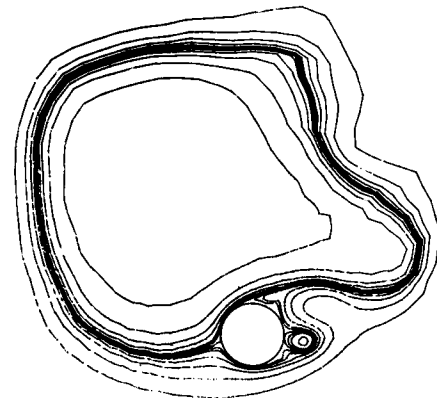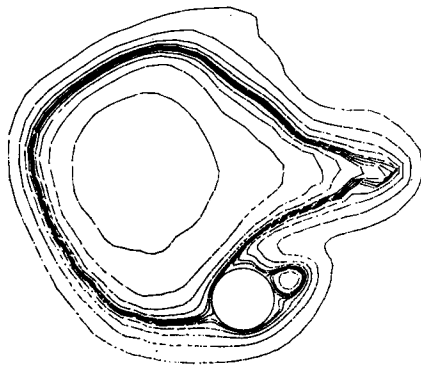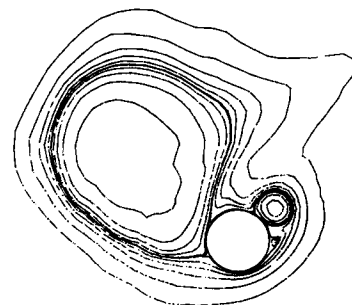DRAG COEFFICIENT
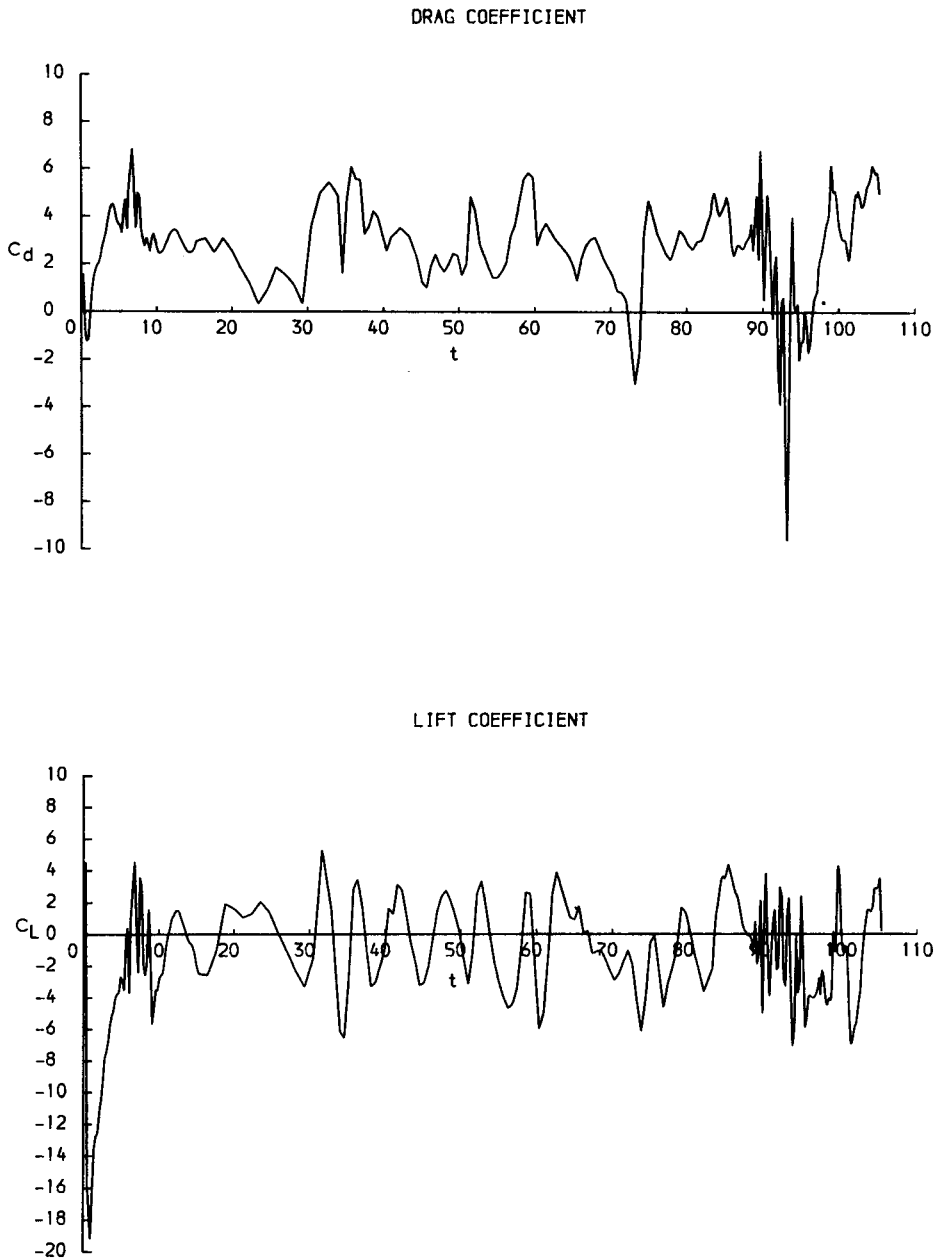
LIFT COEFFICIENT

Figure 24. Drag and lift coefficients: $Re = 1000$, $Kc = 12$

ROUGH MESH RESULTS FOR ORBITAL FLOW PAST A CYLINDER

There is surprisingly good qualitative agreement between the results obtained from the hybrid and rough schemes. Not only does the flow exhibit similar characteristics, but the drag and lift coefficients have the same form with time.

Figure 26 shows the variations in C_d and C_L with time for a Reynolds number of 100 over a
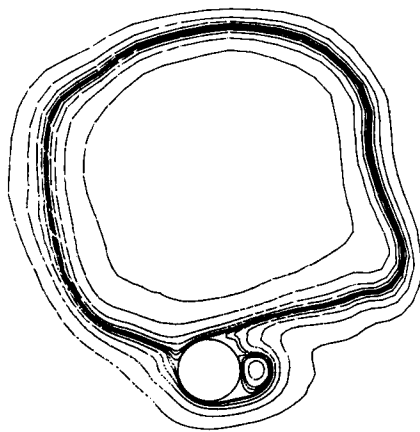
$t = 81 \cdot 842$

$t = 84 \cdot 181$

$t = 85 \cdot 350$

$t = 86 \cdot 520$

$t = 87 \cdot 689$

$t = 88 \cdot 859$

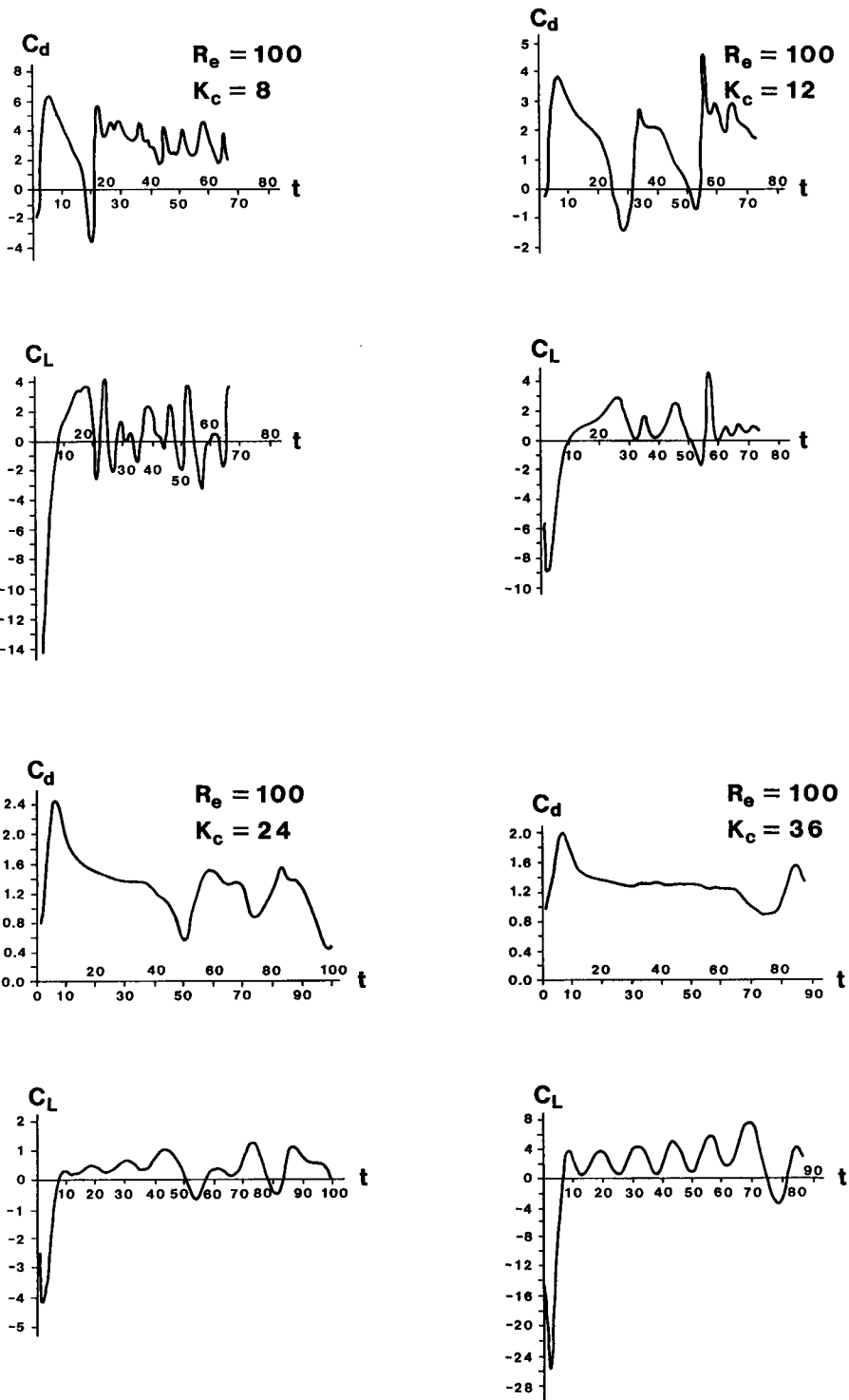Figure 25. Stream-function contours: $Re = 1000$, $Kc = 12$

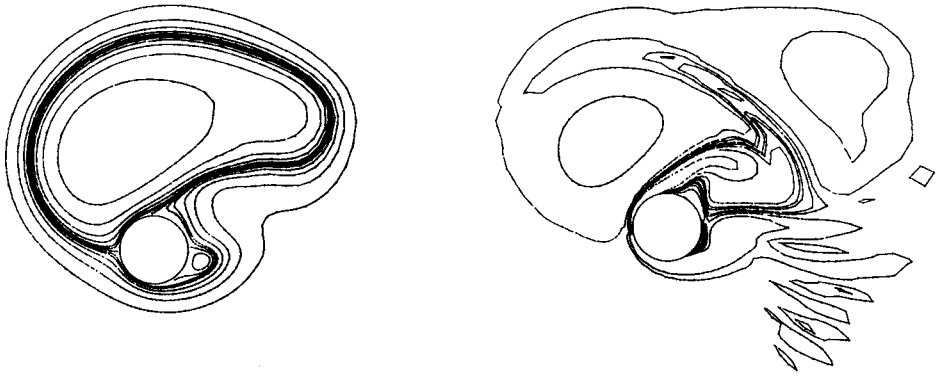Figure 26. Drag and lift coefficients: $Re = 100$, $Kc = 8, 12, 24$ and 36

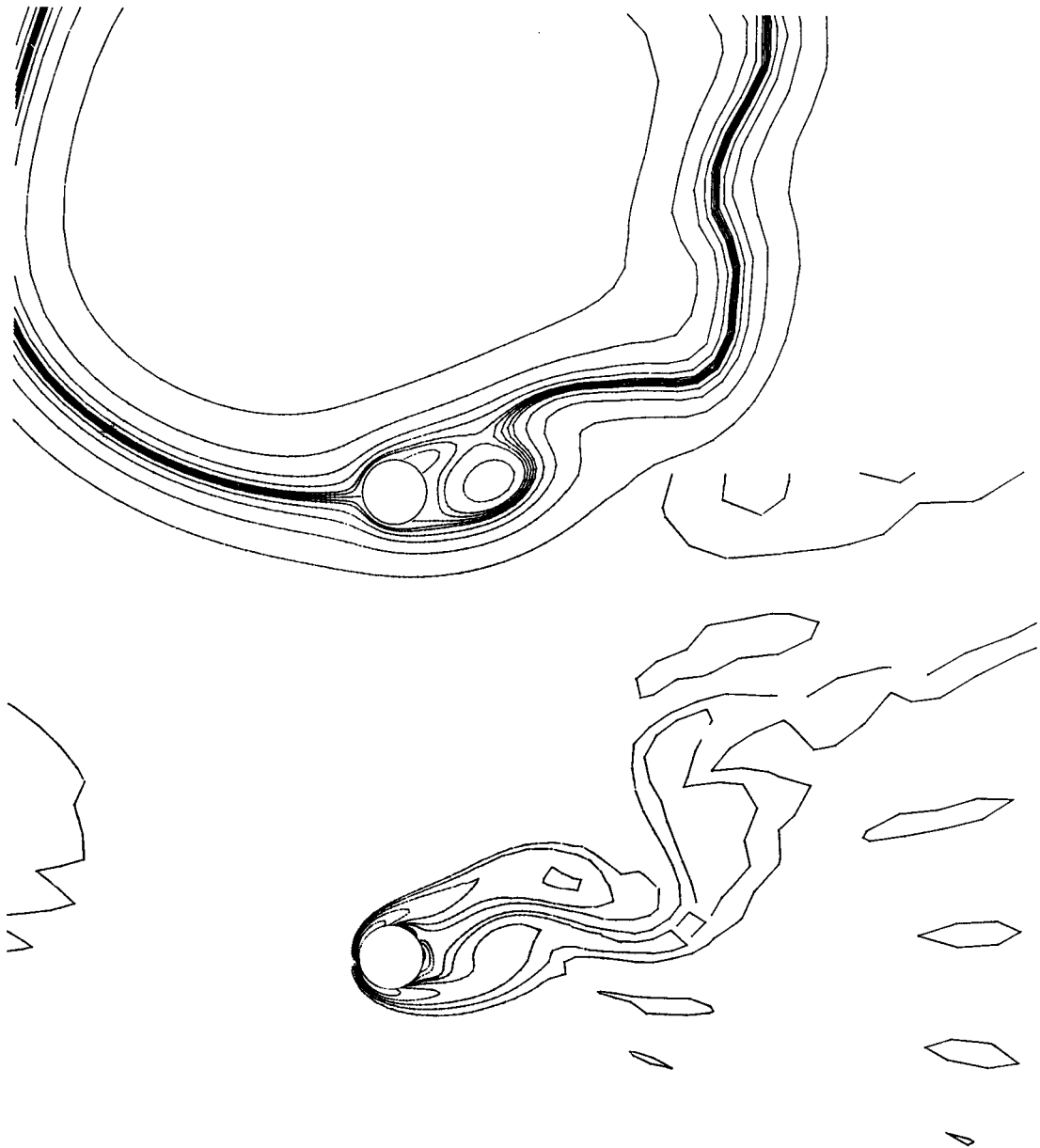Figure 27. Stream-function and vorticity contours: $Re = 100$, $Kc = 8$, $t = 25$

Figure 28. Stream-function and vorticity contours: $Re = 100$, $Kc = 36$, $t = 65$
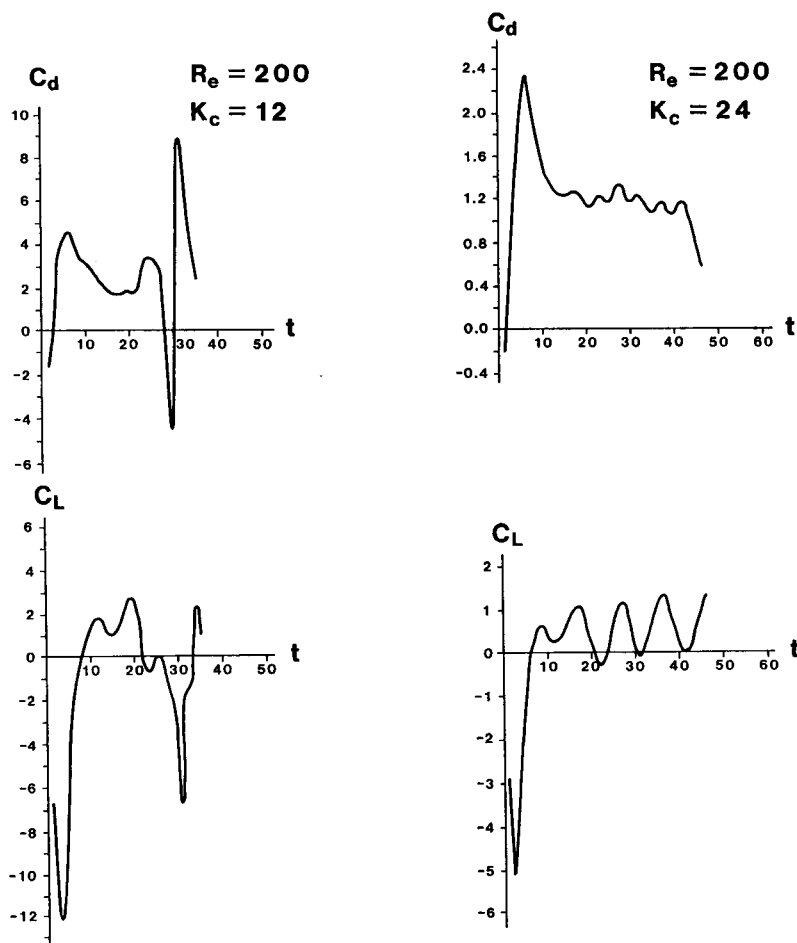
Figure 29. Drag and lift coefficients: $Re = 200$, $Kc = 12$ and 24

range of Keulegen–Carpenter numbers from 8 to 36. At the lowest value of 8, inertia is the dominant force component. After the first cycle there are large fluctuations in both drag and lift as the vortices rotate around the orbit while being deflected outwards. Vortex shedding occurs rapidly and corresponds to a Strouhal number of 0·4. The flow pattern seems disorganized, as shown in Figure 27.

Increasing the Keulegan–Carpenter number through the intermediate range from 12 to 24 has the effect of lowering the Strouhal number to almost 0·2. The fluctuations that result when early detached vortices collide with the cylinder are less dramatic. With a large Keulegan–Carpenter number of 36 the impact of the first vortex is relatively small. After some time there is evidence of a curved Karman-type vortex street which agrees closely with flow visualizations obtained by Chaplin[29] (see Figure 28). In addition, the mean drag coefficient and the amplitude of the fluctuating lift coefficient become smaller with increasing Keulegan–Carpenter number.

Similar results were obtained by varying the Keulegan–Carpenter number from 12 to 36 for a Reynolds number of 200. The vortices that leave the cylinder are larger, and so affect the drag and lift coefficients more. The coefficients obtained at the early stages of the flow development for Keulegan–Carpenter numbers of 12 and 24, are given in Figure 29.

Orbital flow with a Keulegan–Carpenter number of 12 can promote vortex shedding at a low Reynolds number of 40. This is due to the pronounced asymmetry of the wake.

CONCLUSIONS

The results obtained, using both rough and hybrid meshes, compare favourably with those presented by Thoman and Szewczyk[7,22] for stationary and rotating cylinders in uniform flow. The rough mesh has the advantage of needing less computational time than the hybrid mesh. However, boundary layer profiles are not obtained with the rough mesh, and also separation points cannot be modelled properly. Even so, useful information on the hydrodynamic processes is obtained cheaply. The drag coefficient was consistently overpredicted by the hybrid mesh. This is perhaps due to the detached vortices not being dissipated by viscosity rapidly enough. However, the hybrid scheme enabled the separation points to be determined from consideration of the velocity profiles through the boundary layers—a most important advantage. The hybrid mesh scheme presented here uses a finite-difference quotient method for the inner region which results in improved spatial accuracy within the boundary layer.

For intermediate and low Keulegan–Carpenter numbers the flow sequence is as follows. At first, surface vorticity dominates the flow. A vortex detaches from behind the cylinder and moves around the orbit, eventually colliding with the cylinder causing a sudden reduction in drag. Meanwhile, other vortices detach from the cylinder and, after some time, there are several vortices moving around the orbit. The positions and strengths of these vortices influence the shape of the orbit, distorting it from circular to pear-shaped, elliptical, 'rectangular' or other configurations. These vortices gradually spiral away from the centre of the orbit and their cumulative presence eventually prevents any from colliding with the cylinder. The angular positions of the stagnation and separation points are also sensitive to the arrangement of vortices in the flow at any particular instant. This would suggest that the use of discrete vortex models in which the separation points are fixed is unsuitable for orbital flow simulation.

Good qualitative agreement is achieved between results obtained from the hybrid and rough schemes and flow visualizations (see Chaplin[29] and Coutanceau and Ménard[25]) from the rough grid results the mean drag coefficient and the amplitude of the fluctuating lift coefficient reduce with increasing Keulegan–Carpenter number. Inertia seems to dominate low Keulegan–Carpenter number flows. At high Keulegan–Carpenter numbers, a Karman vortex street is established and drag is the dominant force.

Although finite-difference Navier–Stokes models are invalid for the post-critical range of Reynolds numbers usually encountered when considering wave loading on offshore structures, they do give useful information at low Reynolds numbers where the flow is laminar. It is reasonable for the results from these models to be extrapolated in order to cover the range of 'sub-critical' Reynolds numbers in which the boundary layers remain laminar, although there is turbulence in the wake. Discrete vortex models suffer from empiricism and Navier–Stokes models incorporating turbulence are beyond present capabilities. Therefore, laminar finite-difference Navier–Stokes models are most useful for this type of flow problem.

REFERENCES

1. A. Borthwick, 'Comparison between two, finite-difference schemes for computing the flow around a cylinder', *Int. j. numer. methods fluids*, **6**, 275–290 (1986).
2. A. Borthwick, 'Orbital flow past a cylinder', *Ph. D. Thesis*, University of Liverpool, July 1982.
3. P. K. Stansby, 'An inviscid model of vortex shedding from a circular cylinder in steady and oscillatory far flows', *Proc. Inst. Civ. Eng.*, **63**, 865 (1977).
4. P. K. Stansby, 'Mathematical modelling of vortex shedding from cirular cylinders in planar oscillatory flows, including effects of harmonics and response', *Proc. Symposium of Mechanics of Wave-Induced Forces on Cylinders*, Bristol, U.K., September 1978.
5. A. J. Raudkivi and R. A. Callander, *Advanced Fluid Mechanics*, Arnold, 1975.
6. P. Holmes and J. R. Chaplin, 'Wave loads on Horizontal cylinders', *Proc. 16th Int. Conf. Coastal Engineering*, **3**, 2449–2460 (1978).
7. D. C. Thoman and A. A. Szewczyk, 'Time-dependent viscous flow over a circular cylinder', *Physics of Fluids Supplement*, **12**, 76–86 (1969).
8. C. L. Lin and S. C. Lee, 'Transient state analysis of separated flow around a sphere', *International Journal of Computers and Fluids*, **1**, 235–250 (1973).
9. J. S. Son and T. J. Hanratty, 'Numerical solutions of the flow around a cylinder at Reynolds numbers of 40, 200 and 500, *J. Fluid Mech.*, **35**, 369–386 (1969).
10. G. Martinez, 'Caractéristiques dynamiques et themiques de l'ecoulement autour d'un cylindre circulaire a nombres de Reynolds moderes', *Doctor-Ingenieur Thesis*, L'Institute National Polytechnique de Toulouse, France, June 1979.
11. C. L. Lin, D. Pepper and S. Lee, 'Numerical Methods for separated flow solutions around a circular cylinder', *AIAA Journal*, **14**, (7), 900–907 (1976).
12. H. Schlichting, *Boundary Layer Theory*, McGraw-Hill, New York, 6th edn, 1968; 7th edn, 1979.
13. P. J. Roache, *Computational Fluid Dynamics*, Hermosa Publishers, Albuquerque, NM 1972, p. 434.
14. D. W. Peaceman and H. H. Rachford, Jr., 'The numerical solution of parabolic and elliptic differential equations', *Journal of the Society of Industrial and Applied Mathematics*, **3**, 28–41 (1955).
15. E. L. Wachpress, *Iterative Solution of Elliptic Systems*, Prentice-Hall, Englewood Cliffs, New Jersey, 1966.
16. S. K. Dey, 'Numerical solution of non linear implicit finite difference equations of flow problems by perturbed iterations', *Computational Fluid Dynamics, Lecture Series 4*, 1978.
17. D. B. Spalding, 'A novel finite difference formulation for differential expressions involving both first and second derivatives', *Int. j. numer. methods eng.*, **4**, 551–559 (1972).
18. A. K. Runchall, 'Convergence and accuracy of three finite-difference schemes for a two-dimensional conduction and convection problem', *Int. j. numer. methods eng.*, **4**, 541–550 (1972).
19. H. Ha Minh, G. Martinez and H. Boisson, 'Détermination de schémas aux différences finies pour un probléme convection-diffusion en fonction du nombre de Péclet local', *Rapport Interne*, IMF Toulouse, M3-14, April 1978.
20. S. C. R. Dennis, J. D. Hudson and N. Smith, 'Steady laminar forced convection from a circular cylinder at low Reynolds numbers', *Physics of Fluids*, **11**, (5), 933–940 (1968).
21. S. C. R. Dennis and Gau-Zu Chang, 'Numerical solutions for steady flow past a circular cylinder at Reynolds numbers up to 100', *J. Fluid Mech.*, **42**, (3), 471–489 (1970).
22. D. C. Thoman, 'Numerical solutions of time dependent two-dimensional flow of a viscous incompressible fluid over stationary and rotating cylinders', *Ph. D. Thesis*, Department of Mechanical Engineering, University of Notre Dame, Indiana, August 1966.
23. W. M. Collins and S. C. R. Dennis, 'Flow past an impulsively started circular cylinder', *J. Fluid Mech.* **60**, 105–127 (1973).
24. H. M. Badr, and S. C. R. Dennis, 'Time-dependent viscous flow past an impulsively started rotating and translating circular cylinder', *J. Fluid Mech.*, **158**, 447–488 (1985).
25. M. Coutanceau and C. Ménard, 'Influence of rotation on the near-wake development behind an impulsively started circular cylinder', *J. Fluid Mech.*, **158**, 399–446 (1985).
26. W. M. Swanson, 'An experimental investigation of the two-dimensional Magnus effect', Department of Mechanical Engineering Case Institute of Technology, December 1956.
27. A. Thom, 'Effects of discs on the air forces on a rotating cylinder', *ARC R and M 1623*, 1934.
28. W. R. Sears and D. P. Telionis, 'Boundary layer separation in unsteady flow', *SIAM J. Appl Math*, **28**, 215–235 (1975).
29. J. R. Chaplin, 'Boundary layer separation from a cylinder in waves', *International Symposium on Hydrodynamics in Ocean Engineering*, Norwegian Institute of Technology, Trondheim, 1981, pp. 645–666.